Quantifying variability, source, and transport of CO over the Himalayas and Tibetan Plateau

3   Youwen Sun [1], Hao Yin [1], Yuan Cheng [2]*, Qianggong Zhang [3, 4]*, Bo Zheng [5]*, Justus Notholt [6],

4   Xiao Lu [7], Cheng Liu [8, 9, 10, 11, 1], Yuan, Tian [12], and Jianguo Liu [1]

5   (1 *Key Laboratory of Environmental Optics and Technology, Anhui Institute of Optics and Fine*

6   *Mechanics, HFIPS, Chinese Academy of Sciences, Hefei 230031, China*)

7   (2 *State Key Laboratory of Urban Water Resource and Environment, School of Environment,*

8   *Harbin Institute of Technology, Harbin 150090, China*)

9   (3 *Key Laboratory of Tibetan Environment Changes and Land Surface Processes, Institute of*

10 *Tibetan Plateau Research, Chinese Academy of Sciences, Beijing,100101, China*)

11 (4 *CAS Center for Excellence in Tibetan Plateau Earth Sciences, Beijing, 100101, China*)

12 (5 *Laboratoire des Sciences du Climat et de l'Environnement, CEA-CNRS-UVSQ, UMR8212, Gif-*

13 *sur-Yvette, France*)

14 (6 *University of Bremen, Institute of Environmental Physics, P. O. Box 330440, 28334 Bremen,*

15 *Germany*)

16 (7 *School of Engineering and Applied Sciences, Harvard University, Cambridge, MA 02138, USA*)

17 (8 *Center for Excellence in Regional Atmospheric Environment, Institute of Urban Environment,*

18 *Chinese Academy of Sciences, Xiamen, 361021, China*)

19 (9 *Department of Precision Machinery and Precision Instrumentation, University of Science and*

20 *Technology of China, Hefei, 230026, China*)

21 (10 *Key Laboratory of Precision Scientific Instrumentation of Anhui Higher Education Institutes,*

22 *University of Science and Technology of China, Hefei, 230026, China*)

23 (11 *Anhui Province Key Laboratory of Polar Environment and Global Change, University of*

24 *Science and Technology of China, Hefei, 230026, China*)

25 (12 *Anhui University Institutes of Physical Science and Information Technology, Hefei 230601,*

26 *China*)

27 Correspondence: Yuan Cheng (ycheng@hit.edu.cn), Qianggong Zhang (qianggong.zhang@itpcas.

28 ac.cn) and Bo Zheng (bo.zheng@lsce.ipsl.fr)

29 **Abstract:**

30   Atmospheric pollutants over the Himalayas and Tibetan Plateau (HTP) have potential

31 implications for accelerating the melting of glaciers, damaging air quality, water sources and

32 grasslands, and threatening climate on regional and global scales. Improved knowledge of the

33 variabilities, sources, drivers, and transport pathways of atmospheric pollutants over the HTP is

34 significant for regulatory and control purpose. In this study, we first quantify the variability, source,

35 and transport of CO over the HTP by using in situ measurement, GEOS-Chem model tagged CO

36 simulation, and atmospheric circulation pattern techniques. Diurnal, seasonal, and interannual

37 variability of CO over the HTP are investigated with ~ 6 years (January 2015 to July 2020) of surface

38 CO measurements in eight cities over the HTP. Annual mean of surface CO volume mixing ratio

39 (VMR) over the HTP varied over 318.3 ± 71.6 to 901.6 ± 472.2 ppbv, and a large seasonal cycle was

40 observed with high levels of CO in the late autumn to spring and low levels of CO in summer to

41 early autumn. The diurnal cycle is characterized by a bimodal pattern with two maximums in later

42 morning and midnight, respectively. Surface CO VMR from $2015 - 2020$ in most cities over the

1   HTP showed negative trends. The in situ CO measurements are for the first time used to assess the
2   performance of GEOS-Chem full-chemistry model for the specifics of the HTP. Generally, GEOS-
3   Chem can capture the measured variability of low CO levels but shows large discrepancies in high
4   CO levels. Distinct dependencies on a short lifetime species of NO_2 almost in all cities over the HTP
5   were observed, implying local emissions to be predominant. By turning off the emission inventories
6   within the HTP in GEOS-Chem tagged CO simulation, the relative contribution of long range
7   transport was evaluated. The results disclosed that transport ratios of primary anthropogenic source,
8   primary biomass burning (BB) source, and secondary oxidation source to the surface CO VMR over
9   the HTP varied over 35 to 61%, 5 to 21%, and 30 to 56%, respectively. The anthropogenic
10 contribution is dominated by the South Asia and East Asia (SEAS) region throughout the year (58%
11 to 91%). The BB contribution is dominated by the SEAS region in spring (25 to 80%) and the Africa
12 (AF) region in July – February (30 – 70%). This study concluded that the anthropogenic and
13 oxidation sources originating either local or in SEAS region dominated the surface CO over the
14 HTP, which is different from the black carbon that is mainly attributed to BB source from SEAS
15 region. The decreasing trends in surface CO VMR since 2015 in most cities over the HTP are
16 attributed to the reduction in local and transported CO emissions in recent years.

17 **1 Introduction**

18   The Himalayas and Tibetan Plateau (HTP), also named the 'Third Pole' (TP), is an important
19 region for climate change studies due to several reasons. Due to its unique feature for interactions
20 among the atmosphere, biosphere, hydrosphere, and cryosphere, the HTP is referred to as an
21 important indicator of regional and global climate change (Pu et al., 2007;Yao et al., 2012;Zhang et
22 al., 2015). The HTP stores a large amount of ice masses on the planet and provides the headwater
23 of many Asian rivers which contribute water resource to over 1.4 billion people and it thus is referred
24 to as the 'Water Tower of Asia' (Xu et al., 2008;Immerzeel et al., 2010;Gao et al., 2019;Kang et al.,
25 2019). The glaciers and snowmelt over the HTP can potentially modify the regional hydrology,
26 contribute to global sea-level rise, and trigger natural hazards which may threaten the health and
27 wealth of many population (Singh and Bengtsson, 2004;Barnett et al., 2005;Immerzeel et al.,
28 2010;Kaser et al., 2010;Bolch et al., 2012;Yao et al., 2012;Gao et al., 2019). The HTP has an average
29 altitude of about 4000 m above sea level (a.s.l.), which highly elevates topography of the earth
30 system and imposes profound effects on global atmospheric circulation and climate change (Ye and
31 Wu, 1998;Wu et al., 2012;Zhang et al., 2015;Kang et al., 2019). The HTP is also of great interest
32 for satellite and model validation, since many satellites have problems in trace gas retrieval in this
33 region due to high surface albedo at this high altitude (Park et al., 2007a;Park et al., 2007b).
34 Meanwhile, the extreme climate conditions, and the variability between clean and polluted
35 conditions, are a challenge for current climate models (Ye et al., 2012;Zhang et al., 2015).

36   Since the population level is very low, the HTP has long been regarded as atmospheric
37 background with negligible local anthropogenic emissions (Yao et al., 2012;Kang et al., 2019).
38 However, the HTP is surrounded by East Asia and South Asia which include many intensive
39 anthropogenic and natural emission source regions (Zhang et al., 2015;Kang et al., 2019). The
40 transport of polluted air masses from the highly populated area in northern India with its industry
41 and agriculture can have a strong impact on the composition of the atmosphere (Cong et al.,
42 2009;Kang et al., 2019). Furthermore, the Asian monsoon has a strong influence on the dynamics
43 and transport pathways in the HTP (Zhang et al., 2015;Kang et al., 2019). Reanalysis results based

on glacial ice cores and lake sediments have revealed distinguishable anthropogenic disturbances from Asian emissions since the 1950s (Wang et al., 2008;Cong et al., 2013;Zhang et al., 2015;Kang et al., 2016;Kang et al., 2019). Convective transport around the HTP areas has also been verified by satellite observations, chemical model simulations, flask sampling analyses, and in situ measurements of some key atmospheric compositions. These atmospheric compositions include CO (Park et al., 2007a;Park et al., 2007b), CH_4 (Xiong et al., 2009), HCN (Randel et al., 2010), PAN (Zhang et al., 2009;Ungermann et al., 2016;Xu et al., 2018), O_3 (Yin et al., 2017;Xu et al., 2018), black carbon (BC) (Zhang et al., 2015), and aerosol (Cong et al., 2007;Cong et al., 2009). Furthermore, urbanization, industrialization, land use, and infrastructure construction over the HTP have expanded rapidly in recent years, which could also emit air pollutants into the atmosphere (Ran et al., 2014).

The ecosystem over the HTP is sensitive and fragile under the extreme alpine condition. These exogenous and local atmospheric pollutants have potential implications for accelerating the melting of glaciers, damaging air quality, water sources and grasslands, and threatening climate on regional and global scales (Pu et al., 2007;Xu et al., 2009;Yao et al., 2012;Kang et al., 2016;Yin et al., 2019a;Yin et al., 2020;Yin et al., 2019b) . Efforts have been made to understand the variabilities of atmospheric pollutants over the HTP. However, due to the logistic difficulties and poor accessibility of the vast HTP, most studies are based on episodic measurements in specific regions or at widely dispersed sites (Kang et al., 2019). An inter-comparison of these data and deductions may show large inconsistencies and uncertainties because the reported individual studies have often relied on different instruments and techniques (Kang et al., 2019). As a result, the variabilities, sources, drivers, and transport pathways of atmospheric pollutants over the HTP are still poorly understood.

Carbon monoxide (CO) is one of the most critical atmospheric pollutant which not only threatens human health but also plays a vital role in atmospheric chemistry (Zhang et al., 2019;Zheng et al., 2019). CO has a long atmospheric residence time of a few months and is therefore established as a key tracer for air pollution and transport in the atmosphere (Holloway et al., 2000;Zheng et al., 2019). Natural sources such as biomass burning (BB) and anthropogenic sources such as vehicle exhausts, industrial activities, and coal combustions can emit CO directly into the atmosphere (Stremme et al., 2013;Fisher et al., 2017). These CO emissions are mainly attributed to incomplete combustion (Holloway et al., 2000;Stremme et al., 2013). Furthermore, the atmospheric oxidation of methane (CH_4) and numerous nonmethane VOCs (NMVOCs) provides additional important sources of atmospheric CO (Fisher et al., 2017). The major CO sink in the troposphere is oxidation via reaction with hydroxyl radicals (OH). Since CO is heavily involved in the relationship between atmospheric chemistry and climate forcing, it is crucial to investigate its atmospheric burden, variability, and potential drivers over the HTP. CO over the HTP may originate from various source regions and sectors, improved knowledge of their relative contributions to CO variability over the HTP is also significant for regulatory and control purpose.

In this study, we first quantify the variability, source, and transport of CO over the HTP by using in situ measurement, GEOS-Chem model tagged CO simulation, and atmospheric circulation pattern techniques. Diurnal, seasonal, and interannual variability of CO over the HTP are investigated with multiyear time series of surface CO measurements in eight cities over the HTP. The in situ measurements are for the first time used to assess the performance of GEOS-Chem full-chemistry model for the specifics of the HTP. The GEOS-Chem model is further run in a tagged CO mode to quantify relative contribution of long range transport to the observed CO variability over

the HTP. The three-dimensional (3D) transport pathways of CO originated in various source regions and sectors to the HTP are finally determined by the GEOS-Chem simulation, back trajectories analysis and atmospheric circulation pattern.

The next section describes site description and the surface in situ CO and meteorological data, the methodology used to estimate the interannual trend of surface CO, and the GEOS-Chem simulation used for source attribution. Section 3 reports the results for surface CO variability over the HTP on different time scales. Section 4 reports the results for GEOS-Chem model evaluation. Section 5 reports the results for source attribution using GEOS-Chem tagged CO simulation and atmospheric circulation pattern. We conclude the study in Section 6.

2 Methods and data

2.1 Site description

Surface in situ CO measurements in eight cities over the HTP are involved in this study. The geolocations of these cities are shown in Fig. 1 and summarized in Table 1. Ngari locates in the western, Diqing and Qamdo locate in the eastern, and the rest cities all locate in central eastern of the HTP. Ngari, Shigatse, Lhasa, Shannan, and Nyinchi are adjacent to the Himalayas region, and Naqu, Qamdo, and Diqing are relatively far away from the Himalayas region. Generally, these cities represent the most developed and populated areas over the HTP. The altitude of these cities ranges from 3.1 to 4.5 km a.s.l. and the population ranges from 110 to 770 thousand. The surface pressure of these cities is about 600 hPa or less throughout the year (Table 1). Typically, all these cities are formed at flat valleys with the surrounding mountains rising to more than 5.0 km a.s.l., and keep continuous expansion and development over time. These cities are characterized by a typical climate regime in high mountain regions, and is dry and cold in most of the year. Due to the high altitude and thin air, the solar radiations over these cities are stronger than those over other cities at the same latitude around the globe (Ran et al., 2014).

General atmospheric circulation over these cities are typically influenced by three synoptic systems: the warm and wet air masses during the monsoon season in summer, the South Asian anticyclone that controls the upper troposphere and above, and the subtropical mid-latitude westerlies in winter (Yao et al., 2012;Ran et al., 2014;Yin et al., 2017). Inhibited by surrounding mountains, local mountain peak-valley wind systems facilitate the accumulation of atmospheric pollutants near the ground under low wind speed conditions (Kang et al., 2019).

2.2 Surface CO data and meteorological data

Routine in situ measurement of surface air qualities over the HTP started in 2015, which are organized by the China National Environmental Monitoring Center (CNEMC) network funded by the Chinese Ministry of Ecology and Environment (http://www.cnemc.cn/en/, last access: 22 March 2020).The CNEMC network has monitored six surface air pollutants (including CO, O_3, NO_2, SO_2, PM_{10}, and $PM_{2.5}$) at 23 sites in eight cities in Ngari, Lhasa, Naqu, Diqing, Shigatse, Shannan, Nyingchi, and Qamdo over the HTP (Table 1). Each city has at least two measurement sites. Surface CO volume mixing ratio (VMR) measurements at all sites are based on similar gas correlation filter infrared analyzers (http://www.cnemc.cn/en/, last access: 22 March 2020). The hourly mean datasets have covered the period from January 2015 to present for all measurement sites in the eight cities (Table 1). We first applied filter criteria following that of (Lu et al., 2019) to remove unreliable measurements. The resulting measurements at all measurement sites in each city are then averaged

1 to obtain a city representative dataset.

2   The 3D back trajectories calculated using HYbrid Single-Particle Lagrangian Integrated
3 Trajectory (HYSPLIT) model (http://ready.arl.noaa.gov/HYSPLIT.php, last accessed on 23 May
4 2020) are used to determine the transport trajectories (Wang, 2014;Draxler et al., 2020). The input
5 gridded meteorological data were from the Global Data Assimilation System (GDAS-1) operated
6 by the US National Oceanic and Atmospheric Administration (NOAA) with a horizontal resolution
7 of 1°latitude × 1°longitude and 23 vertical grids from 1000 to 20 hPa
8 (https://ready.arl.noaa.gov/gdas1.php, last accessed on 23 May 2020). In this study, calculation and
9 analysis for all back trajectories are based on the TrajStat module (Wang, 2014)
10 (http://meteothink.org/index.html, last accessed on 1 July 2020).

11 **2.3 Regression model for CO trend**
12   We have used a bootstrap resampling model to determine the seasonality and interannual
13 variability of surface CO VMR over the HTP. The resampling methodology follows that of
14 (Gardiner et al., 2008), where a 3rd Fourier series plus a linear function was used to fit multiyear
15 time series of surface CO VMR biweekly mean. All measurements are averaged by two weeks to
16 lower the residual and improve the fitting correlation. The regression model is expressed by Eqs. (1)
17 and (2):

18 $$Y^{meas}(t) = Y^{mod}(t) + \varepsilon(t) \tag{1}$$

19 $$Y^{mod}(t) = A_0 + A_1 t + A_2 \cos\left(\frac{2\pi t}{365}\right) + A_3 \sin\left(\frac{2\pi t}{365}\right) + A_4 \cos\left(\frac{4\pi t}{365}\right) + A_5 \sin\left(\frac{4\pi t}{365}\right) \tag{2}$$

20 $$d\% = \frac{Y^{meas}(t) - Y^{mod}(t)}{Y^{mod}(t)} \times 100 \tag{3}$$

21 where $Y^{meas}(t)$ and $Y^{mod}(t)$ represent the measured and fitted surface CO VMR time series,
22 respectively. A_0 is the intercept, A_1 is the annual growth rate, and A_1/A_0 is the interannual trend
23 discussed below. In this study, we incorporated the errors arising from the autocorrelation in the
24 residuals into the uncertainties in the trends following the procedure of (Santer et al., 2008). The A_2
25 $- A_5$ parameters describe the seasonal cycle, t is the measurement time elapsed since January 2015,
26 and $\varepsilon(t)$ represents the residual between the measurements and the fitted results. Fractional
27 differences of measured CO VMR time series relative to their seasonal mean values represented by
28 $Y^{mod}(t)$ were referred to as seasonal enhancements and were calculated as equation (3).

29 **2.4 GEOS-Chem simulation**
30   Two types of GEOS-Chem model simulations were involved in this study. GEOS-Chem model
31 version 12.2.1 was first ran in a standard full-chemistry mode to be evaluated by the in situ CO
32 measurements. The GEOS-Chem model was then ran in a standard tagged CO mode to quantify
33 relative contribution of long range transport to the observed CO variability over the HTP (Bey et
34 al., 2001) (http://geos-chem.org, last access on 14 May 2020). Both types of simulations were driven
35 by the Goddard Earth Observing System-Forward Processing (GEOS-FP) meteorological fields
36 with a downgraded horizontal resolution of 2° latitude × 2.5° longitude and 72 vertical grids from
37 surface to 0.01 hPa. Surface variables and planetary boundary layer height (PBLH) were
38 implemented in 1 hr interval and other variables were in 3 hr interval. The GEOS-Chem simulation
39 outputs 47 (tagged CO mode) or 72 (full-chemistry mode) vertical layers of CO VMR concentration
40 ranging from the surface to 0.01 hPa with a horizontal resolution of 2° × 2.5° and a temporal

1   resolution of 1 hr. We spun up the model for one year (January 2014 to January 2015) to remove the

2   influence of the initial conditions. We only considered the surface CO simulations for the grid boxes

3   containing the eight cities over the HTP.

4   Global fossil fuel and biofuel emissions were from the Community Emissions Data System

5   (CEDS) inventory (Hoesly et al., 2018) which overwrites regional emissions over the US by

6   National Emission Inventory (NEI), Canada by Canadian Criteria Air Contaminant, Mexico by

7   (Kuhns et al., 2005), Europe by European Monitoring and Evaluation Program (EMEP), East Asia

8   and South Asia by MIX inventory (Li et al., 2017;Zheng et al., 2018;Lu et al., 2019), and Africa by

9   DICE-Africa inventory (Wiedinmyer et al., 2016). Global BB emissions are derived from Global

10   Fire Assimilation System (GFAS) v1.2 (Kaiser et al., 2012;Di Giuseppe et al., 2018). The soil NO_x

11   emissions were from (Hudman et al., 2010;Hudman et al., 2012). Biogenic emissions were from the

12   Model of Emissions of Gases and Aerosols from Nature (MEGAN version 2.1) inventory (Guenther

13   et al., 2012). Wet deposition followed that of (Liu et al., 2001) and dry deposition was calculated by

14   the resistance-in-series algorithm (Wesely, 1989;Zhang et al., 2001). The photolysis rates were

15   obtained from the FAST-JX v7.0 photolysis scheme (Bian and Prather, 2002). A universal

16   tropospheric-stratospheric Chemistry (UCX) mechanism was implemented (Eastham et al., 2014).

17   In GEOS-Chem tagged CO simulation, the monthly mean OH fields obtained from a previous

18   standard full-chemistry simulation were used. Furthermore, the improved secondary CO production

19   scheme of (Fisher et al., 2017) was implemented, which adopts secondary CO production rates from

20   CH_4 and NMVOCs oxidation. These secondary production rates were also derived from a previous

21   standard full-chemistry simulation. The GEOS-Chem tagged CO simulation includes the tracers of

22   primary anthropogenic (fossil fuel + biofuel) and BB sources, and secondary oxidations from CH_4

23   and NMVOCs. Descriptions of all these tracers are summarized in Table 2 and the geographical

24   definitions of all source regions are shown in Fig. 1.

25   **3 Surface CO variability over the HTP**

26   **3.1 Diurnal cycle**

27   Diurnal cycles of surface CO VMR over the HTP within the period of 2015 − 2020 are shown

28   in Fig. 2. The surface CO magnitudes and the hour-to-hour variations in Naqu, Qamdo, and Diqing

29   are higher than those in other cities in all seasons. Furthermore, the daily peak-to-trough contrast in

30   Naqu, Qamdo, and Diqing are also larger than those in other cities. The highest surface CO hourly

31   mean are typically observed in Naqu in all seasons except in the second half day (after 12:00 local

32   time (LT)) in autumn and winter (September-October-November/December-January-February

33   (SON/DJF)), when the highest surface CO values are observed in Qamdo.

34   Diurnal cycles of surface CO VMR in all cities generally show a bimodal pattern in all seasons.

35   For all cities, two diurnal maximums are generally observed during 9:00 to 11:00 LT in the daytime

36   and 21:00 to 23:00 LT in the nighttime in all seasons. The timings of the daytime diurnal maximum

37   in spring and summer (March-April-May/June-July-August (MAM/JJA)) in all cities are 1 to 2

38   hours earlier than those in SON/DJF (Table 3). But the timings of the nighttime diurnal maximum

39   in MAM/JJA in all cities are 1 to 2 hours later than those in SON/DJF. On average, the diurnal hour-

40   to-hour variation of surface CO VMR over the HTP spanned a large range of -47.7% to 50.6%

41   depending on region, season, and measurement time. The diurnal patterns of CO in all cities over

42   the HTP were similar to those in other cities in China (Yin et al., 2019b;Zhao et al., 2016). Surface

43   CO VMR hourly mean in Naqu, Qamdo, and Diqing varied over 455.8 ± 257.8 to 1485.1 ± 1104.7

ppbv, while other cities varied over 256.4 ± 177.1 to 650.0 ± 430.7 ppbv (Table 3). The Class 1 limit for the hourly mean CO concentration in China is 10 mg m^{-3} (8732.1 ppbv) and all hourly mean CO VMRs from 2015 − 2020 over the HTP were below this limit (http://www.cnemc.cn/en/, last access: 22 March 2020).

3.2 Seasonal cycle

Seasonal cycle of surface CO VMR over the HTP within the period of 2015 to 2020 are shown in Fig. 3. As generally observed in most cities over the HTP, surface CO VMR showed clear seasonal features: (1) high levels of surface CO VMR occur in the late autumn to spring and low levels of surface CO occur in summer to early autumn; (2) the variations in the late autumn to spring are larger than those in summer to early autumn; (3) seasonal cycles of surface CO VMR in most cities show a bimodal pattern, i.e., a large seasonal peak occurs around November − December and a small seasonal peak occurs around April − May.

Surface CO VMR monthly mean and month−to−month variations in Naqu, Qamdo, and Diqing are higher than those in other cities in all seasons. Furthermore, the peak−to−trough contrast in Naqu, Qamdo, and Diqing were also larger than those in other cities. Surface CO VMR monthly mean over the HTP varied over a large range of 206.8 ± 93.5 to 1887.1 ± 1132.0 ppbv depending on season and region (Table 3), where Naqu, Qamdo, and Diqing varied over 419.0 ± 221.2 to 1887.1 ± 1132.0 ppbv, and other cities varied over 206.8 ± 93.5 to 759.4 ± 473.8 ppbv (Table 3).

3.3 Interannual variability

Biweekly mean time series of surface CO VMR over the HTP from 2015 to 2020 along with the fitted results by using the regression model $Y^{mod}(t)$ are shown in Fig. 4. Generally, the measured and fitted surface CO VMR over the HTP are in good agreement with a correlation coefficient (r) of 0.81 − 0.93. The measured features in terms of seasonality and interannual variability can be reproduced by the regression model. Seasonal enhancements calculated as equation (3) disclosed that large seasonal enhancements typically occur around November − December and April − May which correspond to the timings of the seasonal peaks for most cities. The trend in surface CO VMR from 2015 to 2020 over the HTP spanned a large range of (-21.6 ± 4.5) % to (11.9 ± 1.38) % per yr, indicating a regional representative of each dataset. Surface CO VMR in six out of eight cities, i.e., Ngari, Lhasa, Shannan, Naqu, Qamdo, and Diqing, showed negative trends. The largest decreasing trends were observed in Qamdo and Naqu, which showed decreasing trends of (-16.98 ± 4.37) % and (-21.6 ± 4.5) % per yr, respectively. Surface CO in two out of eight cities, i.e., Shigatse and Nyingchi, showed positive trends. A large increasing trend of (11.9 ± 1.38) % per yr was observed in Shigatse.

Surface CO VMR annual mean over the HTP varied over 318.3 ± 71.6 to 901.6 ± 472.2 ppbv depending on year and region (Table 3), where Naqu, Qamdo, and Diqing varied over 531.4 ± 156.8 to 901.6 ± 472.2 ppbv, higher than those in other cities which varied over 318.3 ± 71.6 to 446.1 ± 138.5 ppbv (Table 3). The annual mean concentrations of surface CO over the HTP were compared with those from other cities in China. All cities over the HTP except Naqu and Qamdo can be ranked as a few of the top-level cities with the best air quality. Naqu and Qamdo were ranked as the middle-level cities with fair to poor air quality (http://www.cnemc.cn/en/, last access: 22 March 2020).

4 Model evaluation over the HTP

1   The performance of the GEOS-Chem model has been evaluated with available observations
2   over various regions in China and surroundings in previous studies from different perspectives such
3   as surface O_3 concentration in urban regions over China (Lu et al., 2019), tropospheric CO column
4   over eastern China (Chen et al., 2009;Sun et al., 2020b) and Pacific (Yan et al., 2014), tropospheric
5   averaged HCHO concentration over eastern China (Sun et al., 2020a), stratospheric NO_2 partial
6   column (Yin et al., 2019a) and HCl partial column over eastern China (Yin et al., 2020). So far
7   GEOS-Chem model evaluation over the complex topography and meteorology of the HTP is not
8   found in the literature. Here we first use multiyear time series of surface CO VMR over the HTP to
9   evaluate the model performance in the specifics of the HTP. Model evaluation in each region over
10   the HTP is performed through two steps. First, the mean measurement−to−model ratio (hereafter
11   scaling factor) during 2015 − 2020 is scaled to the GEOS-Chem simulations, which is used to
12   evaluate the performance of the GEOS-Chem with respect to reproducibility of the measured
13   amplitude. Second, a linear function is used to fit the scaled model−to−measurement data pairs,
14   which is used to evaluate the performance of the GEOS-Chem with respect to reproducibility of the
15   measured variability.

16   Depending on regions, scaling factors ranging from 0.76 to 1.74 were obtained. Specifically,
17   the GEOS-Chem simulations over the HTP underestimated the measurements by 13.3% to 74%
18   except for the simulations in Nyinchi which overestimated the measurements by 24%. The largest
19   GEOS-Chem vs. measurement differences occur in Qamdo and Naqu, with underestimations of 66%
20   and 74%, respectively. The least GEOS-Chem vs. measurement difference occurs in Shigatse with
21   an underestimation of 13.3%. Correlation plots for the scaled model−to− measurement data pairs in
22   each region over the HTP are shown in Fig. 5, where only data pairs with fractional differences of
23   less than 50% were considered. These selected data pairs are in good agreement with a correlation
24   coefficient (r) of 0.72 − 0.9, which account for about 61.3% to 90.7% of the total measurements
25   depending on regions (Fig. A1). For the scaled model−to−measurement data pairs with fractional
26   differences of larger than 50%, we consider that the measured surface CO features cannot be
27   reproduced by the GEOS-Chem. These discrepant data pairs typically occur in high levels of surface
28   CO in DJF or MAM, which account for 9.3 − 38.7% of the total measurements depending on regions.

29   As a result, GEOS-Chem can capture the measured variability of low CO levels but shows
30   large discrepancies in high CO levels. These GEOS-Chem vs. measurement differences over the
31   HTP were mainly attributed to the underestimation of local anthropogenic CO emissions by bottom-
32   up inventories and also to the coarse spatial resolution of the GEOS-Chem model grid cells. The
33   amount of residential energy use, including fossil fuels and biofuels used for cooking and heating,
34   is not recorded for the Tibet in current energy statistics yearbooks, therefore bottom-up inventories
35   tend to underestimate anthropogenic CO emissions over the HTP (Zheng et al., 2019). This can be
36   shown by the CO emission distribution over the HTP from the MEIC inventory in Fig. A2, which
37   shows that both the spatial distribution and seasonality of CO emission over the HTP are not in good
38   agreement with the in situ measurements. Besides, the coarse spatial resolution of the GEOS-Chem
39   simulations homogenizes CO concentrations within each $0.25° \times 0.3125°$ model grid cell. The
40   simulation results represent mean concentrations in the grid box containing the measurement sites
41   and at the grid-mean elevation, which could cause significantly bias near complex terrain (Yan et
42   al., 2014). Especially, the studied regions represent the most developed and populated areas over
43   the HTP, which are surrounded by large areas of rolling mountains with sparsely interspersed farms,
44   pasture or residency. The horizontal transport and vertical mixing schemes simulated by the GEOS-

Chem model at coarse spatial resolutions are difficult to match surface measurement sites. Regional difference in surface CO levels could aggravate the inhomogeneity within the selected GEOS-Chem model grid, and thus aggravate the difference between modeled and measured CO concentrations.

Considering the difference between the measurement and the model simulation over HTP, the GEOS-Chem model is only used for investigating the influence of long range transport. In subsequent study, we turn off the emission inventories within the HTP in the GEOS-Chem tagged CO simulation and assess the relative contribution of each tracer. Contributions of all tracers are averaged by month to further reduce the uncertainty in statistical analysis.

5 Source attribution

5.1 Local emission

The air quality in a city is influenced by local emission which is spatially differentiated by energy consumption, economic development, industry structure, and population. All studied cities over the HTP have achieved rapid economic and population growth in recent years (Ran et al., 2014;Yin et al., 2019b). For example, Lhasa's gross domestic product (GDP) in 2018 was 29 times higher than that of 2001, and the population had increased by more than 230 thousand in 17 years (Yin et al., 2019b). Correlation plots of surface CO versus NO_2 daily mean VMR time series from $2015 - 2020$ in eight cities over the HTP are shown in Fig. 6. The results show that NO_2 and CO concentrations were correlated in all cities (r ranges from $0.49 - 0.86$) throughout the year. The overall good correlations between these two gas pollutants suggested common sources of ΔNO_2 and ΔCO in these cities. As a short lifetime species (a few hours), the emitted NO_2 is heavily weighted toward the direct vicinity of local emission regions. As a result, local emissions are important sources of CO in all cities. However, the slope $\Delta NO_2/\Delta CO$ and the degree of the correlation in each city are different, indicating the energy consumption and the CO pollution of local sources in these cities are different, and additional sources of CO could exist, e.g., from long range transport or oxidation from CH_4 and NMVOCs originating either nearby or in distant areas.

The emission from coal-burning for heating was thought to be the dominant sources of primary gas pollutants in Lhasa in recent years (Ran et al., 2014;Yin et al., 2019b). A large portion of sole source results in the highest correlation between NO_2 and CO in Lhasa. In contrast, Qamdo, Naqu, and Diqing are surrounded by alpine farmlands and pastures. Historically, post-harvest crop residue (e.g., highland barley straws and withered grass) was often burned by local farmers to fertilize the soil for next planting season. As a fine fuel, post-harvest crop residue was often burned directly in the field in large piles and smolder for weeks. These seasonal crop residue burning behaviors typically occur in the cold season which could cause a high level of CO emission in this period. Furthermore, local residents extensively use dry yak dung as fuel for cooking or heating throughout the year which could elevate the background CO level in these regions. As a result, these higher local sources might be an important factor explaining the higher CO magnitude in these regions.

5.2 Long range transport

Monthly mean contributions of anthropogenic, BB, and oxidation from long range transport to the surface CO VMR over the HTP are shown in Fig.7. All statistical results are based on GEOS-Chem tagged CO simulations by turning off the emission inventories within the HTP. Due to the influence of seasonally variable transport and magnitude of the regional emissions, the

1   anthropogenic, BB and oxidation sources are all seasonal and regional dependent. Generally,
2   anthropogenic contributions in June − September and DJF are higher than those in the rest of the
3   year. In contrast, high levels of oxidation contribution occur in JJA/SON and low levels of oxidation
4   contribution occur in MAM/DJF. For BB source, contributions in MAM/DJF are larger than those
5   in JJA/SON. Depending on season and region, relative contributions of anthropogenic, BB, and
6   oxidation transported to the surface CO VMR over the HTP varied over 35 to 61%, 5 to 21%, and
7   30 to 56%, respectively. The combination of anthropogenic and oxidation sources dominated the
8   contribution which varied over 80 to 95% with an average of 89% throughout the year.

9   After normalizing each regional anthropogenic contribution to the total anthropogenic
10   contribution, the normalized relative (NR) contribution of each anthropogenic region to the total
11   anthropogenic associated transport is obtained in Fig.8. The results show that the anthropogenic
12   associated transport is mainly attributed to the influence of anthropogenic sources in South Asia and
13   East Asia (SEAS). The NR anthropogenic contribution in SEAS ranges from 58% in DJF to 91% in
14   SON. In addition, moderate anthropogenic contributions from North America (NA) (10 to 27%),
15   Europe and Boreal Asia (EUBA) (4 to 12%), and rest of world (ROW) (4 to 10%) are also observed
16   in MAM/DJF. By using a similar normalized method, the NR contributions of each BB tracer and
17   oxidation tracer are obtained in Fig.9 and Fig. 10, respectively. The results show that large BB
18   contributions are from the Africa (AF) region in July – February (30 – 70%), the SEAS region in
19   MAM (25 to 80%), and the EUBA region in July – September (15 to 32%). Additional moderate
20   BB contributions are from the South America (SA) region in May – June and September – December
21   (9 to 14%), the Oceania (OCE) region in the second half of the year (5 to 15%), and the NA region
22   in September – December (8 to 19%). Depending on season and region, 45 to 67% of oxidation
23   contribution are attributed to CH_4 oxidation, and 32 to 55% of oxidation contribution are attributed
24   to NMVOCs oxidation. High-level NR contributions of CH_4 oxidation occur in the cold season
25   (November – March) and low-level NR contributions of CH_4 oxidation occur in the warm season
26   (April – October). The NR contributions of NMVOCs oxidation varied over an opposite mode to
27   that of CH_4 oxidation; they maximize in the warm season and minimize in the cold season.

28   **5.3 Transport pathways**
29   The 3D transport trajectories of CO originated in various source regions and sectors to the HTP
30   are identified as bellow. First, the GEOS-Chem tagged CO simulation is applied for determining
31   seasonal NR contribution of each tracer (Figs. 8 and 9). For the tracer with a NR contribution of
32   larger than 30% at a specific time (hereafter enhancement time), the global CO distribution provided
33   by the GEOS-Chem simulation is applied to search for potential CO sources occurring before the
34   enhancement time within 15 days. Then, we generated a variety of back trajectories with various
35   travel times to judge whether these CO emissions are capable of travelling to the measurement
36   region. For instance, with respect to each CO enhancement measured at a specific time, we
37   generated ten back trajectories arriving at 100 m above the ground but with different travel time
38   ranging from 3 to 15 days. If the back trajectories intersect a region where the GEOS-Chem
39   simulation indicates an intensive CO source and the travel duration is within ± 2 hr of the observed
40   enhancement, then this specific CO source could contribute to the observed enhancement over the
41   HTP. The transport trajectories for this CO source are finally determined. Meanwhile, global fire
42   atlas data archived by the Fire Information for Resource Management System (FIRMS) is used to
43   determine if intensive fire events occur around the location of this CO source

1   (https://firms.modaps.eosdis.nasa.gov/download/, last access on 23 April 2020). This CO source is

2   regarded as BB source if concurrent intensive fire numbers are observed. Otherwise, it is regarded

3   as anthropogenic source.

4   Fig. 11 demonstrates travel trajectories of polluted air masses originated in AF, SEAS + OCE,

5   EUBA, and NA regions which arrived at Naqu (31.5°N) over the HTP through long range transport.

6   As the FIRMS global fire map shown (Fig. A3), CO emissions from southern Africa during July –

7   September, central Africa during November – February, central Europe during July – November,

8   Siberia during June – September, and South Asia peninsula during March – May are dominated by

9   BB source. Otherwise, the potential CO sources are dominated by anthropogenic emissions. Fig.12

10   shows the spatial distribution of CO VMR along with the mean horizontal wind vectors at 500 hPa

11   in different seasons. Fig. 13 illustrates the latitude − height and longitude − height distributions of

12   CO VMR along with the 3D atmospheric circulation patterns in different seasons. The 3D transport

13   pathways of CO around the HTP are thus deduced as follows.

14   As indicated by the arrows in Fig. 12 and Fig.13, the strong surface cooling in DJF over the

15   HTP results in divergence and the formation of an enhanced local circulation cell, while in JJA air

16   masses converge toward the HTP from the surroundings triggered by the ascending of strongly

17   heated air masses over the HTP (Zhang et al., 2015). In DJF, the tropical easterlies are weak but the

18   mid-latitude westerlies extend to subtropics (∼ 20°N) near the surface and tropics (~10°N) over

19   middle troposphere (Fig. 13). In the summer monsoon season, the atmospheric circulation patterns

20   around the HTP change dramatically and is dominated by the reversal of surface wind regime in the

21   tropics such as South China Sea, Bay of Bengal, and Arabian Sea (Fig.11 and Fig.13). Meanwhile,

22   the mid-latitude westerlies in JJA recede to the North Temperate Zone (north of 30°N) and the

23   westerly jet center shifts to about 40°N (from about 30°N in DJF). In JJA, the tropical region in the

24   south of the HTP is characterized by the strong easterlies in the upper troposphere and by the

25   southwesterly air flow in the lower troposphere (Fig. 13). The prevailing winds during the transition

26   seasons in MAM and SON are still westerlies (Fig. 13). These above seasonal atmospheric

27   circulation patterns control the CO transport pathway around the HTP. Nevertheless, the transported

28   CO scales to the HTP are also influenced by source location and strength, travel trajectory and

29   elapsed time (Yao et al., 2012;Zhang et al., 2015;Kang et al., 2019).

30   In the SON/DJF, a significant amount of CO from southern SEAS (anthropogenic source),

31   northern AF (BB source), western EUBA, and northern NA (anthropogenic source) can be

32   transported to the HTP along the westerlies in the dry winter monsoon conditions. CO originating

33   in distant regions such as western EUBA and NA reaches a high altitude (to 8 km) during the

34   transport (Fig. 11). However, CO from the densely populated and industrialized areas in eastern

35   China barely reaches the HTP because of strong removal along the transport pathways to the HTP

36   which circles around the Northern Hemisphere along the westerlies during the winter monsoon

37   season (Fig. 12). In MAM, CO emissions from BB sources in SEAS region can be transported to

38   the HTP which is mainly triggered by deep convection followed by northward transport into the

39   mid-latitude westerlies (Liu et al., 2003)(Fig. 13). During the South Asian summer monsoon, the

40   local abundant wet precipitation can remove a large portion of SEAS originated CO but can still

41   affect southwest HTP (Fig. 13). Along strong southeasterly air flow in summer monsoon season,

42   CO from eastern China can be uplifted higher and transported more to the northeast HTP than that

43   in the DJF. In addition, large−scale atmospheric deep convection can loft CO from upwind source

44   regions (e.g., central SA, and Indonesia (within OCE region)) into higher altitudes, where it can be

1 transported to the HTP in SON or DJF. Generally, CO diffusions over the HTP in all seasons are

2 driven by atmospheric deep convection which lofts CO into higher altitudes or by westerlies which

3 transports local emissions far away (Fig. 13).

4 **5.4 Factors drive surface CO variability over the HTP**

5 Temporal CO burden is dependent on the difference between the CO source and sink, which is

6 determined by the accumulated influence of local emission, transport, oxidation generation,

7 environmental capacity, and OH oxidation capability. The environmental capacity is determined by

8 self−clean capability, topography, deposition, and meteorological condition (Hofzumahaus et al.,

9 2009). Generally, the vertical self−clean capability is positively correlated with the PBLH and the

10 horizontal self−clean capability is positively correlated with the wind speed (Rohrer et al., 2014).

11 The OH oxidation capability is positively correlated with temperature and radiation (Rohrer et al.,

12 2014).

13 The bimodal pattern of diurnal cycles for surface CO VMR over the HTP is attributed to the

14 following diurnal accumulation, diffusion and deplete processes. The thin atmosphere over the HTP

15 causes large temperature and radiation differences between day and night (Yin et al., 2017;Kang et

16 al., 2019). The PBLH and OH oxidation capability in the nighttime are much lower than those in

17 the daytime (Ran et al., 2014;Yin et al., 2017;Yin et al., 2019b). The CO emissions over the HTP

18 start to accumulation after sunrise and reach the daytime maximum during rush hours at 8:00 to

19 11:00 LT in the morning. The CO concentration is then decreasing as a result of diffusion or

20 depletion by reactions with OH to form O_3 (Ran et al., 2014;Yin et al., 2019b). Subsequently, CO

21 emissions start to accumulation again during rush hours at 16:00 to 19:00 LT in the afternoon, and

22 reach the nighttime maximum at 21:00 to 23:00 LT due to low PBLH and OH oxidation capability

23 in the nighttime (Ran et al., 2014;Yin et al., 2019b).

24 Similarly, the seasonal cycle of surface CO VMR over the HTP is determined by the seasonal

25 variability of CO source, environmental capacity, and OH oxidation capability. High levels of

26 surface CO VMR in the late autumn to spring can be attributed to low PBLH and OH oxidation

27 capability but high local CO emission and transport in this period, and vice versa for low levels of

28 surface CO VMR in summer to early autumn (Yin et al., 2019b). Specifically, local anthropogenic

29 CO sources in urban regions over the HTP (mainly heating activities) during the colder post-

30 monsoon and winter months are higher than those in other seasons. Meanwhile, the westerlies near

31 the surface in SON/DJF are weaker than those in MAM/JJA, which facilitate the accumulation of

32 atmospheric pollutants (Fig. 13). Furthermore, high levels of CO are observed in the late autumn to

33 spring in neighboring SEAS countries due to intensive anthropogenic emissions or BB practices

34 (Kan et al., 2012;Tiwari et al., 2014;Liu et al., 2018;Gani et al., 2019). These polluted air masses

35 can transport to the HTP region and elevate the local CO level (Fig.13). Thus, apart from local

36 anthropogenic emissions, these transported sources might be an important factor explaining the high

37 CO pollution in winter. In addition, high surface CO level over the HTP may be also associated with

38 a low-pressure system (~ 600 hPa) over the HTP (Fig.13). On the one hand, the ratio CO/CO_2 might

39 shift towards CO because of less O_2, leading to more CO concentration. On the other hand, the

40 produced CO will be distributed in a volume with less air molecules under low air pressure condition,

41 increasing the mixing ratio of CO.

42 Since the crop residue burning emissions result in poor air quality that threatens local terrestrial

43 ecosystems and human health, Chinese government started to ban crop residue burning over China

1 since 2015 and henceforth the crop residue burning events over the HTP decreased dramatically

2 (Sun et al., 2020b) (http://www.chinalaw.gov.cn, last access on 19 June 2020). Meanwhile, the major

3 air pollutant emissions have decreased around the globe in recent years as a consequence of active

4 clean air policies for mitigating severe air pollution problems in the major anthropogenic emission

5 regions, such as China, India, Europe and America (Zheng et al., 2018;Sun et al., 2020a).

6 Furthermore, an elevated BB events in AF, SEAS, and OCE regions were observed at the beginning

7 of the studied years due to the El Niño Southern Oscillation (ENSO) in 2015 (Sun et al., 2020b).

8 All these factors probably drive a decreasing trend in surface CO VMR since 2015 in most cities

9 over the HTP. However, an overall increase in surface CO VMR in Shigatse and Nyingchi since

10 2015 indicated that the decrease in transported CO was overwhelmed by the increase in local CO

11 emissions as a result of the expansion of urbanization, industrialization, land use, and infrastructure

12 construction near the two cities.

6 Concluding remarks

14   In this study, we first quantified the variability, source, and transport of CO over the Himalayas

15 and Tibetan Plateau (HTP) by using in situ measurement, GEOS-Chem model tagged CO simulation,

16 and atmospheric circulation pattern techniques. Diurnal, seasonal, and interannual variability of CO

17 over the HTP are investigated with ~ 6 years (January 2015 to July 2020) of surface CO

18 measurements in eight cities over the HTP. Annual mean of surface CO volume mixing ratio (VMR)

19 over the HTP varied over 318.3± 71.6 to 901.6 ± 472.2 ppbv, and a large seasonal cycle was

20 observed with high levels of CO VMR in the late autumn to spring and low levels of VMR in

21 summer to early autumn. Surface CO VMR burdens and variations in Naqu, Qamdo, and Diqing

22 are higher than those in other cities in all seasons. The diurnal cycle is characterized by a bimodal

23 pattern with two maximums occurring around 9:00 to 11:00 local time (LT) in the daytime and 21:00

24 to 23:00 LT in the nighttime. The trend in surface CO VMR from 2015 to 2020 over the HTP

25 spanned a large range of (-21.6 ± 4.5) % to (11.9 ± 1.38) % per yr, indicating a regional

26 representative of each dataset. However, surface CO VMR from 2015 to 2020 in most cities over

27 the HTP showed negative trends.

28   The in situ measurements are for the first time used to assess the performance of GEOS-Chem

29 full-chemistry model for the specifics of topography and meteorology over the HTP. Generally,

30 GEOS-Chem can capture the measured variability of low CO levels but shows large discrepancies

31 in high CO levels. Distinct dependencies on a short life time species of NO_2 almost in all cities over

32 the HTP were observed, implying local emissions to be predominant. By turning off the emission

33 inventories within the HTP in GEOS-Chem tagged CO simulation, the relative contribution of long

34 range transport was evaluated. The results disclosed that transport ratios of primary anthropogenic

35 source, primary biomass burning (BB) source, and secondary oxidation source to the surface CO

36 VMR over the HTP varied over 35 to 61%, 5 to 21%, and 30 to 56%, respectively. The

37 anthropogenic contribution is dominated by the South Asia and East Asia (SEAS) region throughout

38 the year (58% to 91%). The BB contribution is dominated by the SEAS region in spring (25 to 80%)

39 and the Africa (AF) region in July – February (30 – 70%). Additional important anthropogenic

40 contributions from North America (NA) (10 to 27%) and Europe and Boreal Asia (EUBA) (4 to

41 12%) in spring and winter (MAM/DJF) are also observed. Additional important BB contributions

42 are from the EUBA region in July – September (15 to 32%), the South America (SA) region in May

43 – June and September – December (9 to 14%), the Oceania (OCE) region in the second half of the

year (5 to 15%), and the NA region in September – December (8 to 19%). The decreasing trends in surface CO VMR since 2015 in most cities over the HTP are attributed to the reduction in local and transported CO emissions in recent years.

This study concluded that the anthropogenic and oxidation sources originating either local or in SEAS region dominated the urban surface CO over the HTP, which is different from the black carbon (BC) that is mainly attributed to BB source from SEAS region. This study can also improve knowledge of the variabilities, sources, drivers, and transport pathways of atmospheric pollutants over the HTP and provide guidance for potential regulatory and control actions.

Data availability. Surface CO time series in all cities over the Himalayas and Tibetan Plateau (HTP) and GEOS-Chem tagged CO simulations in this study are available on request.

Author contributions. YS designed the study and prepared the paper with inputs from all coauthors. HY carried out the GEOS-Chem CO simulations. The rest authors contributed to this work via provide constructive comments.

Competing interests. The authors declare that they have no conflict of interest.

Acknowledgements. This work is jointly supported by the National High Technology Research and Development Program of China (No.2019YFC0214802, No.2017YFC0210002, 2018YFC0213201, 2019YFC0214702, and 2016YFC0200404), the National Science Foundation of China (No. 41575021, No. 51778596, No. 41977184, and No.41775025), the Major Projects of High Resolution Earth Observation Systems of National Science and Technology (05-Y30B01-9001-19/20-3), the Sino-German Mobility programme (M-0036), and Anhui Province Natural Science Foundation of China (No. 2008085QD180). We thank the GEOS-Chem team and Tsinghua University, China for providing the latest MEIC inventory. We thank NOAA for providing the HYSPLIT model and GEOS-FP meteorological files. We thank prof. Yaqiang Wang for providing the TrajStat module for air masses back trajectories calculation. We thank prof. Dr. Martyn Chipperfield from university of Leeds and prof. Zhiyuan Cong from Institute of Tibetan Plateau Research, CAS for their invaluable comments for improving this paper. Surface CO time series in all cities over the Himalayas and the Tibetan Plateau are provided by the China National Environmental Monitoring Center (CNEMC) network funded by the Chinese Ministry of Ecology and Environment.

References

Barnett, T. P., Adam, J. C., and Lettenmaier, D. P.: Potential impacts of a warming climate on water availability in snow-dominated regions, Nature, 438, 303-309, 2005.

Bey, I., Jacob, D. J., Yantosca, R. M., Logan, J. A., Field, B. D., Fiore, A. M., Li, Q. B., Liu, H. G. Y., Mickley, L. J., and Schultz, M. G.: Global modeling of tropospheric chemistry with assimilated meteorology: Model description and evaluation, J Geophys Res-Atmos, 106, 23073-23095, 2001.

Bian, H. S., and Prather, M. J.: Fast-J2: Accurate simulation of stratospheric photolysis in global chemical models, J Atmos Chem, 41, 281-296, 2002.

Bolch, T., Kulkarni, A., Kaab, A., Huggel, C., Paul, F., Cogley, J. G., Frey, H., Kargel, J. S., Fujita, K., Scheel, M., Bajracharya, S., and Stoffel, M.: The State and Fate of Himalayan Glaciers, Science, 336, 310-314, 2012.

Chen, D., Wang, Y., McElroy, M. B., He, K., Yantosca, R. M., and Le Sager, P.: Regional CO pollution

and export in China simulated by the high-resolution nested-grid GEOS-Chem model, Atmos Chem Phys, 9, 3825-3839, 2009.

Cong, Z. Y., Kang, S. C., Liu, X. D., and Wang, G. F.: Elemental composition of aerosol in the Nam Co region, Tibetan Plateau, during summer monsoon season, Atmos Environ, 41, 1180-1187, 2007.

Cong, Z. Y., Kang, S. C., Smirnov, A., and Holben, B.: Aerosol optical properties at Nam Co, a remote site in central Tibetan Plateau, Atmos Res, 92, 42-48, 2009.

Cong, Z. Y., Kang, S. C., Gao, S. P., Zhang, Y. L., Li, Q., and Kawamura, K.: Historical Trends of Atmospheric Black Carbon on Tibetan Plateau As Reconstructed from a 150-Year Lake Sediment Record, Environmental Science & Technology, 47, 2579-2586, 2013.

Di Giuseppe, F., Remy, S., Pappenberger, F., and Wetterhall, F.: Using the Fire Weather Index (FWI) to improve the estimation of fire emissions from fire radiative power (FRP) observations, Atmos Chem Phys, 18, 5359-5370, 2018.

Draxler, R. R., Stunder, B., Rolph, G., and Taylor, A.: HYSPLIT4 users guide, NOAA Technical Memorandum ERL ARL, 230, 2020.

Eastham, S. D., Weisenstein, D. K., and Barrett, S. R. H.: Development and evaluation of the unified tropospheric-stratospheric chemistry extension (UCX) for the global chemistry-transport model GEOS-Chem, Atmos Environ, 89, 52-63, 2014.

Fisher, J. A., Murray, L. T., Jones, D. B. A., and Deutscher, N. M.: Improved method for linear carbon monoxide simulation and source attribution in atmospheric chemistry models illustrated using GEOS-Chem v9, Geosci Model Dev, 10, 4129-4144, 2017.

Gani, S., Bhandari, S., Seraj, S., Wang, D. Y. S., Patel, K., Soni, P., Arub, Z., Habib, G., Hildebrandt Ruiz, L., and Apte, J. S.: Submicron aerosol composition in the world's most polluted megacity: the Delhi Aerosol Supersite study, Atmos Chem Phys, 19, 6843-6859, 2019.

Gao, J., Yao, T., Masson-Delmotte, V., Steen-Larsen, H. C., and Wang, W.: Collapsing glaciers threaten Asia's water supplies, Nature, 565, 19-21, 2019.

Gardiner, T., Forbes, A., de Maziere, M., Vigouroux, C., Mahieu, E., Demoulin, P., Velazco, V., Notholt, J., Blumenstock, T., Hase, F., Kramer, I., Sussmann, R., Stremme, W., Mellqvist, J., Strandberg, A., Ellingsen, K., and Gauss, M.: Trend analysis of greenhouse gases over Europe measured by a network of ground-based remote FTIR instruments, Atmos Chem Phys, 8, 6719-6727, 2008.

Guenther, A. B., Jiang, X., Heald, C. L., Sakulyanontvittaya, T., Duhl, T., Emmons, L. K., and Wang, X.: The Model of Emissions of Gases and Aerosols from Nature version 2.1 (MEGAN2.1): an extended and updated framework for modeling biogenic emissions, Geosci Model Dev, 5, 1471-1492, 2012.

Hoesly, R. M., Smith, S. J., Feng, L. Y., Klimont, Z., Janssens-Maenhout, G., Pitkanen, T., Seibert, J. J., Vu, L., Andres, R. J., Bolt, R. M., Bond, T. C., Dawidowski, L., Kholod, N., Kurokawa, J., Li, M., Liu, L., Lu, Z. F., Moura, M. C. P., O'Rourke, P. R., and Zhang, Q.: Historical (1750-2014) anthropogenic emissions of reactive gases and aerosols from the Community Emissions Data System (CEDS), Geosci Model Dev, 11, 369-408, 10.5194/gmd-11-369-2018, 2018.

Hofzumahaus, A., Rohrer, F., Lu, K. D., Bohn, B., Brauers, T., Chang, C. C., Fuchs, H., Holland, F., Kita, K., Kondo, Y., Li, X., Lou, S. R., Shao, M., Zeng, L. M., Wahner, A., and Zhang, Y. H.: Amplified Trace Gas Removal in the Troposphere, Science, 324, 1702-1704, 2009.

Holloway, T., Levy, H., and Kasibhatla, P.: Global distribution of carbon monoxide, J Geophys Res-Atmos, 105, 12123-12147, Doi 10.1029/1999jd901173, 2000.

Hudman, R. C., Russell, A. R., Valin, L. C., and Cohen, R. C.: Interannual variability in soil nitric oxide emissions over the United States as viewed from space, Atmos Chem Phys, 10, 9943-9952, 2010.

1 Hudman, R. C., Moore, N. E., Mebust, A. K., Martin, R. V., Russell, A. R., Valin, L. C., and Cohen, R.
2   C.: Steps towards a mechanistic model of global soil nitric oxide emissions: implementation and
3   space based-constraints, Atmos Chem Phys, 12, 7779-7795, 2012.
4 Immerzeel, W. W., van Beek, L. P. H., and Bierkens, M. F. P.: Climate Change Will Affect the Asian
5   Water Towers, Science, 328, 1382-1385, 2010.
6 Kaiser, J. W., Heil, A., Andreae, M. O., Benedetti, A., Chubarova, N., Jones, L., Morcrette, J. J., Razinger,
7   M., Schultz, M. G., Suttie, M., and van der Werf, G. R.: Biomass burning emissions estimated with
8   a global fire assimilation system based on observed fire radiative power, Biogeosciences, 9, 527-
9   554, 2012.
10 Kan, H. D., Chen, R. J., and Tong, S. L.: Ambient air pollution, climate change, and population health in
11   China, Environment International, 42, 10-19, 2012.
12 Kang, S. C., Huang, J., Wang, F. Y., Zhang, Q. G., Zhang, Y. L., Li, C. L., Wang, L., Chen, P. F., Sharma,
13   C. M., Li, Q., Sillanpaa, M., Hou, J. Z., Xu, B. Q., and Guo, J. M.: Atmospheric Mercury
14   Depositional Chronology Reconstructed from Lake Sediments and Ice Core in the Himalayas and
15   Tibetan Plateau, Environmental Science & Technology, 50, 2859-2869, 2016.
16 Kang, S. C., Zhang, Q. G., Qian, Y., Ji, Z. M., Li, C. L., Cong, Z. Y., Zhang, Y. L., Guo, J. M., Du, W. T.,
17   Huang, J., You, Q. L., Panday, A. K., Rupakheti, M., Chen, D. L., Gustafsson, O., Thiemens, M. H.,
18   and Qin, D. H.: Linking atmospheric pollution to cryospheric change in the Third Pole region:
19   current progress and future prospects, Natl Sci Rev, 6, 796-809, 2019.
20 Kaser, G., Grosshauser, M., and Marzeion, B.: Contribution potential of glaciers to water availability in
21   different climate regimes, P Natl Acad Sci USA, 107, 20223-20227, 2010.
22 Kuhns, H., Knipping, E. M., and Vukovich, J. M.: Development of a United States-Mexico Emissions
23   Inventory for the Big Bend Regional Aerosol and Visibility Observational (BRAVO) Study, Journal
24   of the Air & Waste Management Association, 55, 677-692, 2005.
25 Li, M., Zhang, Q., Kurokawa, J., Woo, J. H., He, K. B., Lu, Z. F., Ohara, T., Song, Y., Streets, D. G.,
26   Carmichael, G. R., Cheng, Y. F., Hong, C. P., Huo, H., Jiang, X. J., Kang, S. C., Liu, F., Su, H., and
27   Zheng, B.: MIX: a mosaic Asian anthropogenic emission inventory under the international
28   collaboration framework of the MICS-Asia and HTAP, Atmos Chem Phys, 17, 935-963,
29   10.5194/acp-17-935-2017, 2017.
30 Liu, H. Y., Jacob, D. J., Bey, I., and Yantosca, R. M.: Constraints from Pb-210 and Be-7 on wet deposition
31   and transport in a global three-dimensional chemical tracer model driven by assimilated
32   meteorological fields, J Geophys Res-Atmos, 106, 12109-12128, 2001.
33 Liu, H. Y., Jacob, D. J., Bey, I., Yantosca, R. M., Duncan, B. N., and Sachse, G. W.: Transport pathways
34   for Asian pollution outflow over the Pacific: Interannual and seasonal variations, J Geophys Res-
35   Atmos, 108, 2003.
36 Liu, T. J., Marlier, M. E., DeFries, R. S., Westervelt, D. M., Xia, K. R., Fiore, A. M., Mickley, L. J.,
37   Cusworth, D. H., and Milly, G.: Seasonal impact of regional outdoor biomass burning on air
38   pollution in three Indian cities: Delhi, Bengaluru, and Pune, Atmos Environ, 172, 83-92, 2018.
39 Lu, X., Zhang, L., Chen, Y., Zhou, M., Zheng, B., Ke, L., Liu, Y., Lin, J., Fu, T.-M., and Zhang, Q.:
40   Exploring 2016–2017 surface ozone pollution over China: source contributions and meteorological
41   influences, Atmos Chem Phys, 19, 8339-8361, 10.5194/acp-19-8339-2019, 2019.
42 Park, M., Randel, W. J., Emmons, L. K., Bernath, P. F., Walker, K. A., and Boone, C. D.: Chemical
43   isolation in the Asian monsoon anticyclone observed in Atmospheric Chemistry Experiment (ACE-
44   FTS) data, Atmospheric Chemistry & Physics Discussions, 7, 757-764, 2007a.

1 Park, M., Randel, W. J., Gettelman, A., Massie, S. T., and Jiang, J. H.: Transport above the Asian summer
2   monsoon anticyclone inferred from Aura Microwave Limb Sounder tracers, Journal of Geophysical
3   Research, 112, D16309, 2007b.
4 Pu, Z. X., Xu, L., and Salomonson, V. V.: MODIS/Terra observed seasonal variations of snow cover over
5   the Tibetan Plateau, Geophys Res Lett, 34, 2007.
6 Ran, L., Lin, W. L., Deji, Y. Z., La, B., Tsering, P. M., Xu, X. B., and Wang, W.: Surface gas pollutants
7   in Lhasa, a highland city of Tibet – current levels and pollution implications, Atmos. Chem.
8   Phys., 14, 10721-10730, 10.5194/acp-14-10721-2014, 2014.
9 Randel, W. J., Park, M., Emmons, L., Kinnison, D., Bernath, P., Walker, K. A., Boone, C., and Pumphrey,
10   H.: Asian monsoon transport of pollution to the stratosphere, ence, 328, 611-613, 2010.
11 Rohrer, F., Lu, K. D., Hofzumahaus, A., Bohn, B., Brauers, T., Chang, C. C., Fuchs, H., Haseler, R.,
12   Holland, F., Hu, M., Kita, K., Kondo, Y., Li, X., Lou, S. R., Oebel, A., Shao, M., Zeng, L. M., Zhu,
13   T., Zhang, Y. H., and Wahner, A.: Maximum efficiency in the hydroxyl-radical-based self-cleansing
14   of the troposphere, Nat Geosci, 7, 559-563, 2014.
15 Santer, B. D., Thorne, P. W., Haimberger, L., Taylor, K. E., Wigley, T. M. L., Lanzante, J. R., Solomon,
16   S., Free, M., Gleckler, P. J., Jones, P. D., Karl, T. R., Klein, S. A., Mears, C., Nychka, D., Schmidt,
17   G. A., Sherwood, S. C., and Wentz, F. J.: Consistency of modelled and observed temperature trends
18   in the tropical troposphere, Int J Climatol, 28, 1703-1722, 2008.
19 Singh, P., and Bengtsson, L.: Hydrological sensitivity of a large Himalayan basin to climate change,
20   Hydrological Processes, 2004.
21 Stremme, W., Grutter, M., Rivera, C., Bezanilla, A., Garcia, A. R., Ortega, I., George, M., Clerbaux, C.,
22   Coheur, P. F., Hurtmans, D., Hannigan, J. W., and Coffey, M. T.: Top-down estimation of carbon
23   monoxide emissions from the Mexico Megacity based on FTIR measurements from ground and
24   space, Atmos Chem Phys, 13, 1357-1376, 2013.
25 Sun, Y., Yin, H., Liu, C., Zhang, L., Cheng, Y., Palm, M., Notholt, J., Lu, X., Vigouroux, C., Zheng, B.,
26   Wang, W., Jones, N., Shan, C., Tian, Y., Hu, Q., and Liu, J.: Mapping the drivers of formaldehyde
27   (HCHO) variability from 2015-2019 over eastern China: insights from FTIR observation and
28   GEOS-Chem model simulation, Atmos. Chem. Phys. Discuss., 2020, 1-24, 10.5194/acp-2020-544,
29   2020a.
30 Sun, Y. W., Liu, C., Zhang, L., Palm, M., Notholt, J., Hao, Y., Vigouroux, C., Lutsch, E., Wang, W., Shan,
31   C. G., Blumenstock, T., Nagahama, T., Morino, I., Mahieu, E., Strong, K., Langerock, B., De
32   Maziere, M., Hu, Q. H., Zhang, H. F., Petri, C., and Liu, J. G.: Fourier transform infrared time series
33   of tropospheric HCN in eastern China: seasonality, interannual variability, and source attribution,
34   Atmos Chem Phys, 20, 5437-5456, 2020b.
35 Tiwari, S., Bisht, D. S., Srivastava, A. K., Pipal, A. S., Taneja, A., Srivastava, M. K., and Attri, S. D.:
36   Variability in atmospheric particulates and meteorological effects on their mass concentrations over
37   Delhi, India, Atmos Res, 145, 45-56, 2014.
38 Ungermann, J., Ern, M., Kaufmann, M., Muller, R., Spang, R., Ploeger, F., Vogel, B., and Riese, M.:
39   Observations of PAN and its confinement in the Asian summer monsoon anticyclone in high spatial
40   resolution, Atmos Chem Phys, 16, 8389-8403, 2016.
41 Wang, X. P., Xu, B. Q., Kang, S. C., Cong, Z. Y., and Yao, T. D.: The historical residue trends of DDT,
42   hexachlorocyclohexanes and polycyclic aromatic hydrocarbons in an ice core from Mt. Everest,
43   central Himalayas, China, Atmos Environ, 42, 6699-6709, 2008.
44 Wang, Y. Q.: MeteoInfo: GIS software for meteorological data visualization and analysis, Meteorol Appl,

1   21, 360-368, 2014.

2   Wesely, M. L.: Parameterization of Surface Resistances to Gaseous Dry Deposition in Regional-Scale
3   Numerical-Models, Atmos Environ, 23, 1293-1304, Doi 10.1016/0004-6981(89)90153-4, 1989.

4   Wiedinmyer, Christine, Marais, Eloise, and A.: Air Quality Impact of Diffuse and Inefficient Combustion
5   Emissions in Africa (DICE-Africa), Environmental Science & Technology: ES&T, 2016.

6   Wu, G. X., Liu, Y. M., He, B., Bao, Q., Duan, A. M., and Jin, F. F.: Thermal Controls on the Asian
7   Summer Monsoon, Sci Rep-Uk, 2, 2012.

8   Xiong, X., Houweling, S., Wei, J., Maddy, E., Sun, F., and Barnet, C.: Methane plume over south Asia
9   during the monsoon season: satellite observation and model simulation, Atmos Chem Phys, 9, 783-
10   794, 2009.

11   Xu, B. Q., Cao, J. J., Hansen, J., Yao, T. D., Joswia, D. R., Wang, N. L., Wu, G. J., Wang, M., Zhao, H.
12   B., Yang, W., Liu, X. Q., and He, J. Q.: Black soot and the survival of Tibetan glaciers, P Natl Acad
13   Sci USA, 106, 22114-22118, 2009.

14   Xu, X. B., Zhang, H. L., Lin, W. L., Wang, Y., Xu, W. Y., and Jia, S. H.: First simultaneous measurements
15   of peroxyacetyl nitrate (PAN) and ozone at Nam Co in the central Tibetan Plateau: impacts from the
16   PBL evolution and transport processes, Atmos Chem Phys, 18, 5199-5217, 2018.

17   Xu, X. D., Lu, C. G., Shi, X. H., and Gao, S. T.: World water tower: An atmospheric perspective, Geophys
18   Res Lett, 35, 2008.

19   Yan, Y. Y., Lin, J. T., Kuang, Y., Yang, D., and Zhang, L.: Tropospheric carbon monoxide over the Pacific
20   during HIPPO: two-way coupled simulation of GEOS-Chem and its multiple nested models, Atmos
21   Chem Phys, 14, 12649-12663, 2014.

22   Yao, T. D., Thompson, L., Yang, W., Yu, W. S., Gao, Y., Guo, X. J., Yang, X. X., Duan, K. Q., Zhao, H.
23   B., Xu, B. Q., Pu, J. C., Lu, A. X., Xiang, Y., Kattel, D. B., and Joswiak, D.: Different glacier status
24   with atmospheric circulations in Tibetan Plateau and surroundings, Nat Clim Change, 2, 663-667,
25   2012.

26   Ye, D. Z., and Wu, G. X.: The role of the heat source of the Tibetan Plateau in the general circulation,
27   Meteorology & Atmospheric Physics, 67, 181-198, 1998.

28   Ye, H., Zhang, R. D., Shi, J. S., Huang, J. P., Warren, S. G., and Fu, Q.: Black carbon in seasonal snow
29   across northern Xinjiang in northwestern China, Environ Res Lett, 7, 2012.

30   Yin, H., Sun, Y. W., Liu, C., Zhang, L., Lu, X., Wang, W., Shan, C. G., Hu, Q. H., Tian, Y., Zhang, C. X.,
31   Su, W. J., Zhang, H. F., Palm, M. A., Notholt, J., and Liu, J. G.: FTIR time series of stratospheric
32   NO_2 over Hefei, China, and comparisons with OMI and GEOS-Chem model data, Opt Express, 27,
33   A1225-A1240, 2019a.

34   Yin, H., Sun, Y. W., Liu, C., Lu, X., Smale, D., Blumenstock, T., Nagahama, T., Wang, W., Tian, Y., Hu,
35   Q. H., Shan, C. G., Zhang, H. F., and Liu, J. G.: Ground-based FTIR observation of hydrogen
36   chloride (HCl) over Hefei, China, and comparisons with GEOS-Chem model data and other ground-
37   based FTIR stations data, Opt Express, 28, 8041-8055, 2020.

38   Yin, X., Foy, B. D., Wu, K., Feng, C., and Zhang, Q.: Gaseous and particulate pollutants in Lhasa, Tibet
39   during 2013–2017: Spatial variability, temporal variations and implications, Environmental
40   Pollution, 253, 2019b.

41   Yin, X. F., Kang, S. C., de Foy, B., Cong, Z. Y., Luo, J. L., Zhang, L., Ma, Y. M., Zhang, G. S., Rupakheti,
42   D., and Zhang, Q. G.: Surface ozone at Nam Co in the inland Tibetan Plateau: variation, synthesis
43   comparison and regional representativeness, Atmos Chem Phys, 17, 11293-11311, 2017.

44   Zhang, J. M., Wang, T., Ding, A. J., Zhou, X. H., Xue, L. K., Poon, C. N., Wu, W. S., Gao, J., Zuo, H. C.,

1 Chen, J. M., Zhang, X. C., and Fan, S. J.: Continuous measurement of peroxyacetyl nitrate (PAN)
2   in suburban and remote areas of western China, Atmos Environ, 43, 228-237, 2009.
3 Zhang, L. M., Gong, S. L., Padro, J., and Barrie, L.: A size-segregated particle dry deposition scheme for
4   an atmospheric aerosol module, Atmos Environ, 35, 549-560, Doi 10.1016/S1352-2310(00)00326-
5   5, 2001.
6 Zhang, Q., Zheng, Y. X., Tong, D., Shao, M., Wang, S. X., Zhang, Y. H., Xu, X. D., Wang, J. N., He, H.,
7   Liu, W. Q., Ding, Y. H., Lei, Y., Li, J. H., Wang, Z. F., Zhang, X. Y., Wang, Y. S., Cheng, J., Liu, Y.,
8   Shi, Q. R., Yan, L., Geng, G. N., Hong, C. P., Li, M., Liu, F., Zheng, B., Cao, J. J., Ding, A. J., Gao,
9   J., Fu, Q. Y., Huo, J. T., Liu, B. X., Liu, Z. R., Yang, F. M., He, K. B., and Hao, J. M.: Drivers of
10   improved PM$_{2.5}$ air quality in China from 2013 to 2017, P Natl Acad Sci USA, 116, 24463-24469,
11   2019.
12 Zhang, R., Wang, H., Qian, Y., Rasch, P. J., Easter, R. C., Ma, P. L., Singh, B., Huang, J., and Fu, Q.:
13   Quantifying sources, transport, deposition, and radiative forcing of black carbon over the Himalayas
14   and Tibetan Plateau, Atmos Chem Phys, 15, 6205-6223, 2015.
15 Zhao, S., Yu, Y., Yin, D., He, J., Liu, N., Qu, J., and Xiao, J.: Annual and diurnal variations of gaseous
16   and particulate pollutants in 31 provincial capital cities based on in situ air quality monitoring data
17   from China National Environmental Monitoring Center, Environment International, 86, 92-106,
18   2016.
19 Zheng, B., Tong, D., Li, M., Liu, F., Hong, C. P., Geng, G. N., Li, H. Y., Li, X., Peng, L. Q., Qi, J., Yan,
20   L., Zhang, Y. X., Zhao, H. Y., Zheng, Y. X., He, K. B., and Zhang, Q.: Trends in China's
21   anthropogenic emissions since 2010 as the consequence of clean air actions, Atmos Chem Phys, 18,
22   14095-14111, 2018.
23 Zheng, B., Chevallier, F., Yin, Y., Ciais, P., Fortems-Cheiney, A., Deeter, M., Parker, R., Wang, Y.,
24   Worden, H., and Yuanhong, Z.: Global atmospheric carbon monoxide budget 2000-2017 inferred
25   from multi-species atmospheric inversions, Earth Syst Sci Data, 11, 1411-1436, 10.5194/essd-11-
26   1411-2019, 2019.

1 **Figures**
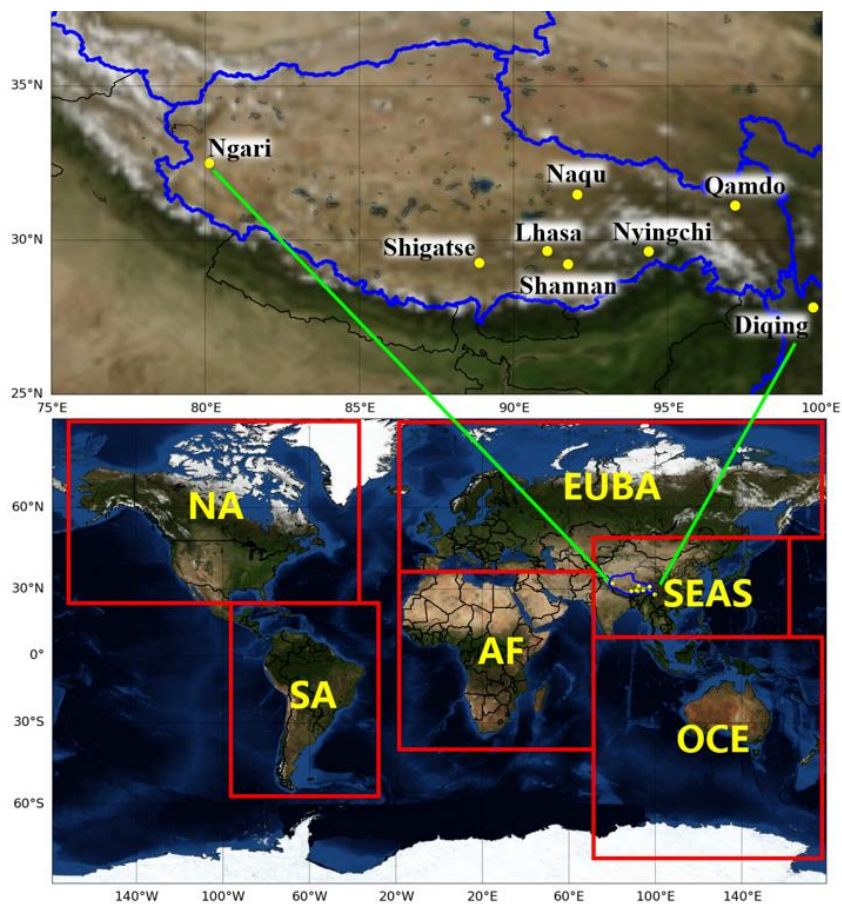
3   Fig. 1. Enlarge view for geolocations of all cities (yellow dots) over the Himalayas and Tibetan Plateau (HTP) (top).
4   Geographical regions implemented in the standard GEOS-Chem tagged CO simulation (bottom). Latitude and
5   longitude definitions are listed in Table 2 .
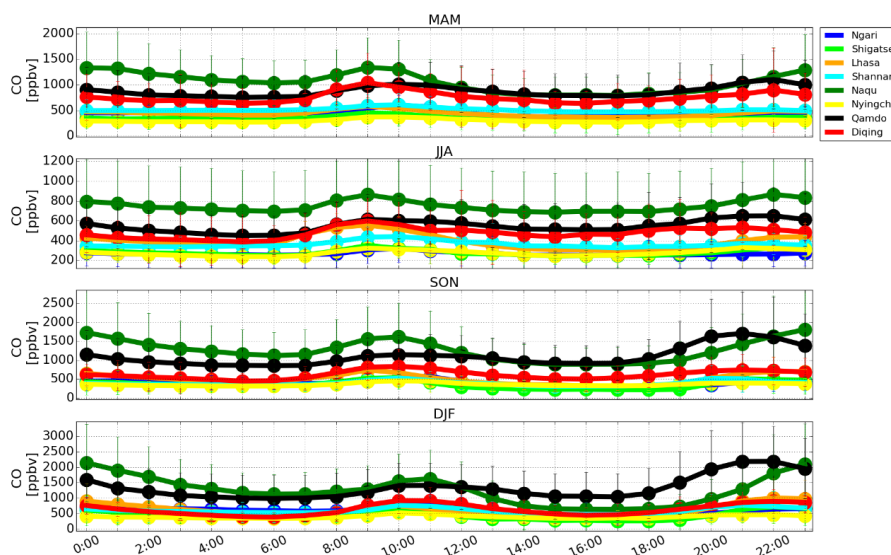
Fig. 2. Diurnal cycles (local time (LT)) of surface CO VMR in four seasons over the Himalayas and Tibetan Plateau
(HTP). Vertical error bar is 1σ standard variation within that hour. Results are based on CO time series from 2015
to 2020 provided by the CNEMC network.
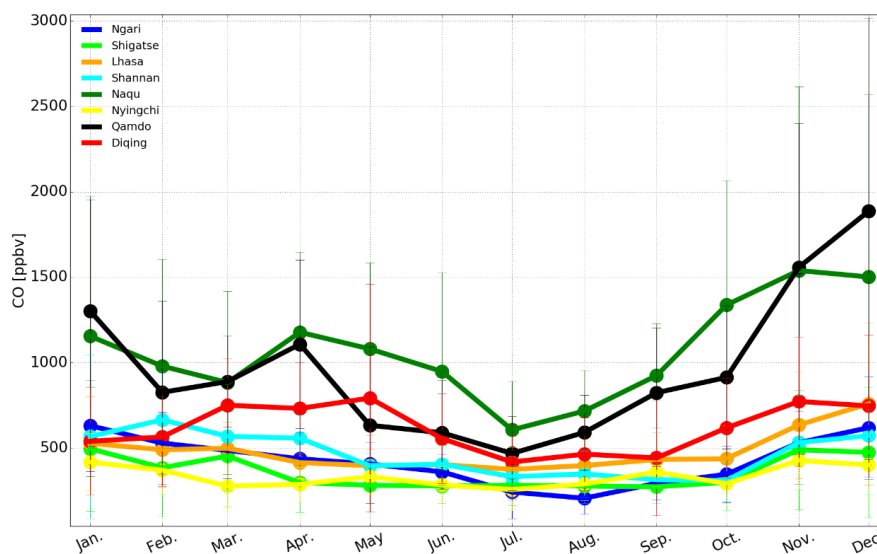
Fig. 3. Monthly mean of surface CO VMR over the Himalayas and Tibetan Plateau (HTP). Vertical error bar
represent 1σ standard variation within that month. Results are based on CO VMR time series from 2015 to 2020
provided by the CNEMC network.
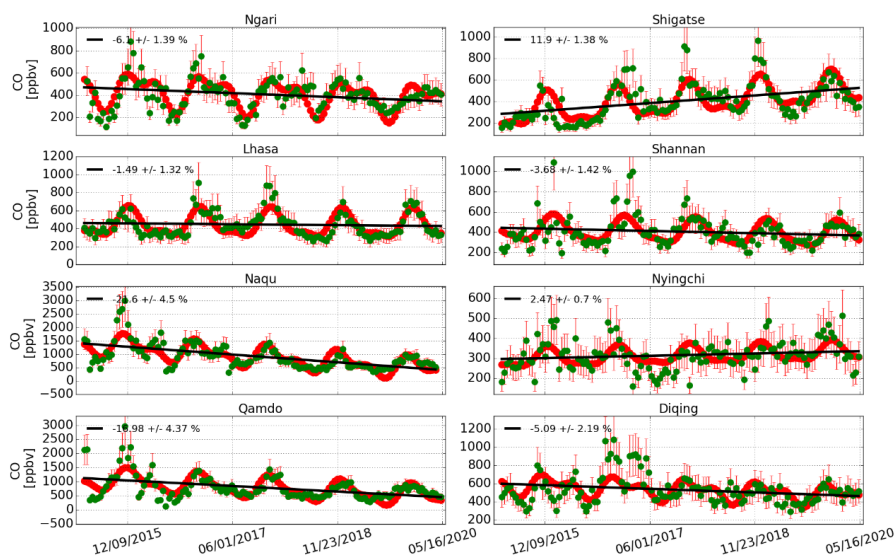
Fig. 4. Interannual variabilities of surface CO from 2015 to 2020 over the Himalayas and Tibetan Plateau (HTP).
Green dots are biweekly mean of *in-situ* surface CO measurements. Vertical red error bar is 1σ standard variation
within the respective two weeks. The seasonality and interannual trend in each city fitted by using a bootstrap
resampling model with a 3rd Fourier series (red dots) plus a linear function (black line) is also shown.
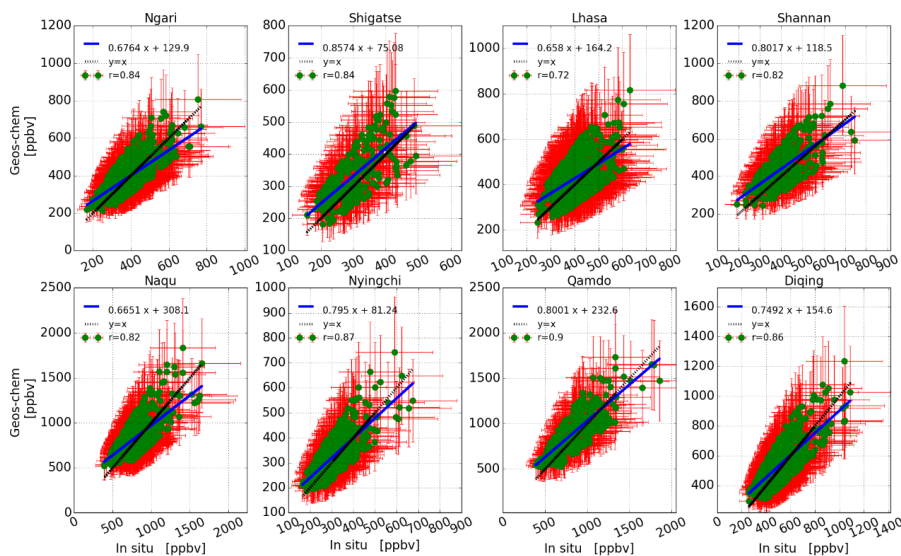
Fig. 5. Correlation plots of surface CO VMR over the Himalayas and Tibetan Plateau (HTP) for scaled GEOS-Chem
model simulation against *in-situ* measurement. Only data pairs with fractional differences of less than 50% were
considered. The blue lines are linear fitted curves of respective scatter points. The black dotted lines denote one-to-
one lines. Vertical error bar represent 1σ standard variation within that day.
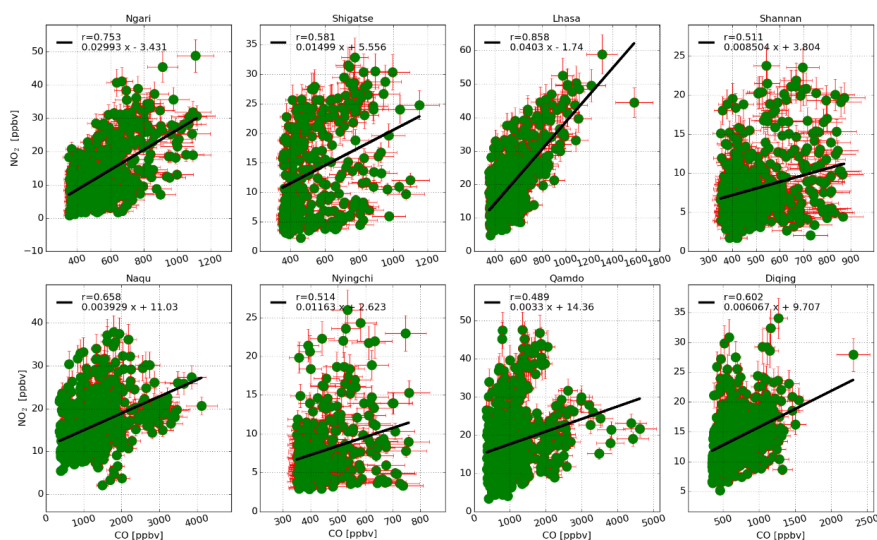
Fig. 6. Correlation plots of surface CO versus NO$_2$ VMR daily mean over the Himalayas and Tibetan Plateau (HTP).
The black line is a linear least-squares fit of respective data. The linear equation of the fit and the resulting correlation
coefficient (r) are shown. Vertical error bar is 1σ standard variation within that day.
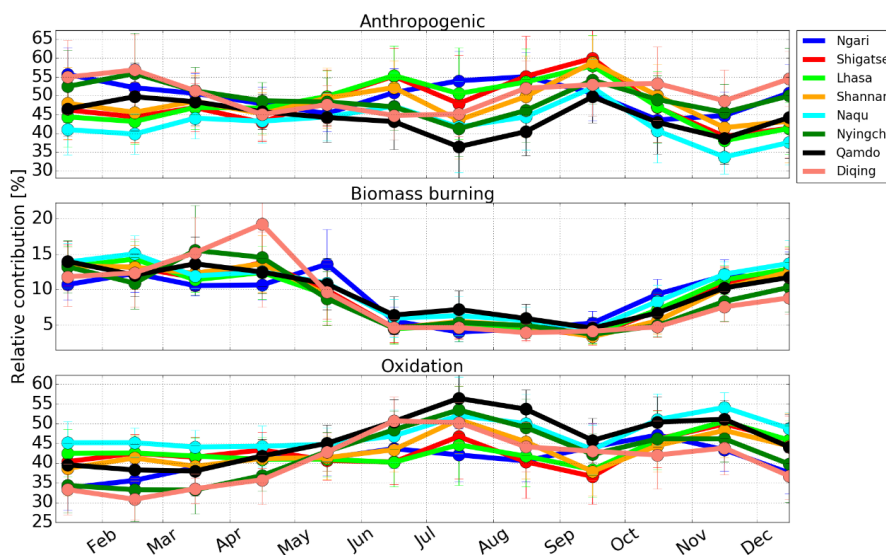
Fig. 7. Monthly mean contributions of anthropogenic, biomass burning (BB) and oxidation transport to the surface
CO VMR over the Himalayas and Tibetan Plateau (HTP). Vertical error bar represent 1σ standard variation within
that month. See Table 2 for description of each tracer.
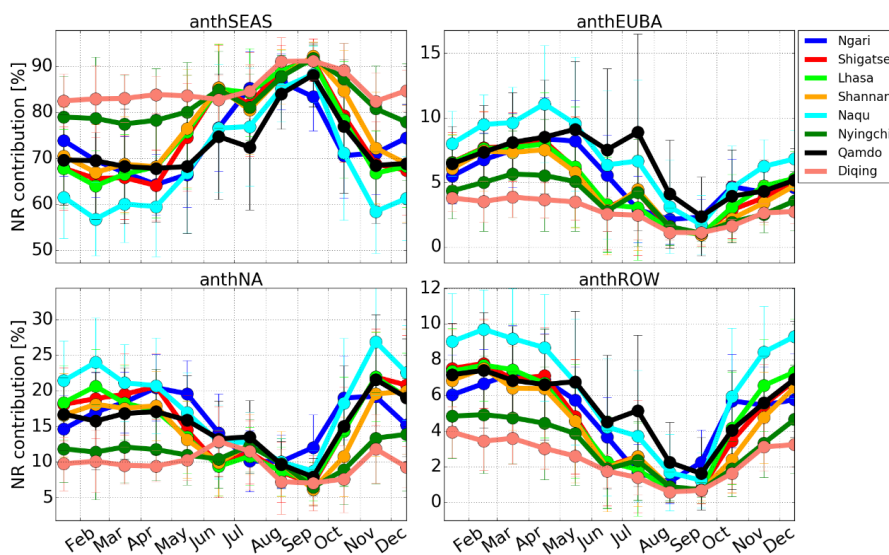
2   Fig. 8. Monthly mean contributions of each geographical anthropogenic tracer to the total anthropogenic associated
3   CO transport to the Himalayas and Tibetan Plateau (HTP). Vertical error bar is 1σ standard variation within that
4   month. See Table 2 for description of each tracer.
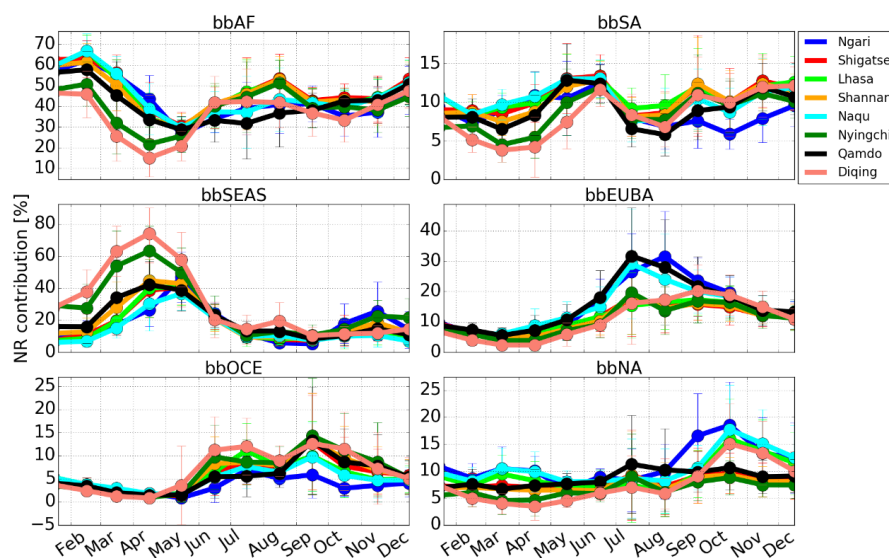
6   Fig. 9. Monthly mean contributions of each geographical BB tracer to the total BB associated CO transport to the
7   Himalayas and Tibetan Plateau (HTP). Vertical error bar represent 1σ standard variation within that month. See
8   Table 2 for description of each tracer.
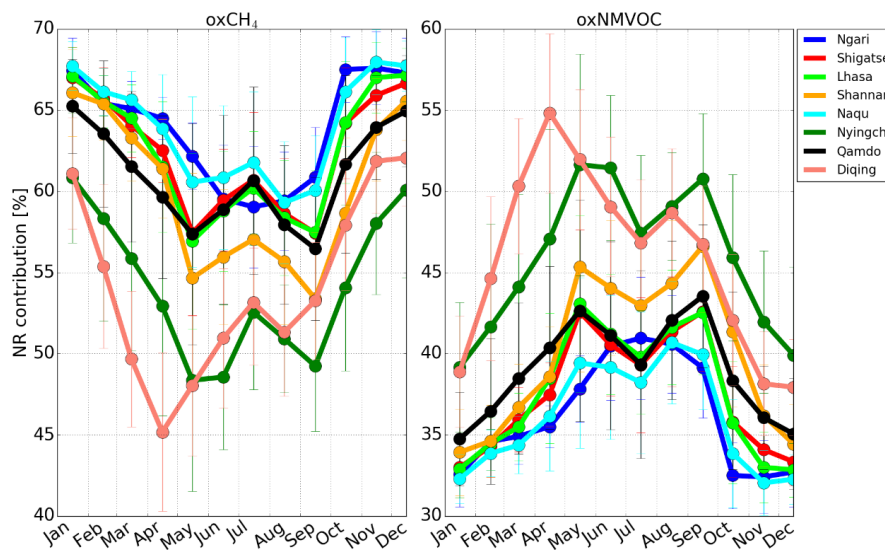
2 Fig. 10. Monthly mean contributions of CH$_4$ and NMVOC oxidations to the total oxidation associated CO transport
3 to the Himalayas and Tibetan Plateau (HTP). Vertical error bar represent 1σ standard variation within that month.
4 See Table 2 for description of each tracer.
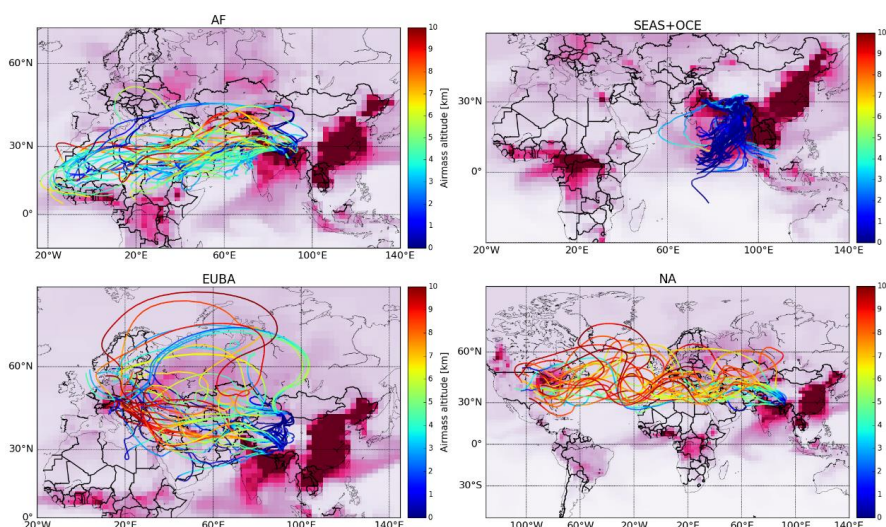
6 Fig. 11. Travel trajectories of polluted air masses originated in AF (SON/DJF), SEAS & OCE (MAM/JJA), EUBA
7 (SON/DJF), and NA (SON/DJF) that reached Naqu (31.5°N) through long range transport. For clarity, only few
8 trajectories are selected for demonstration. Travel times are 13, 7, 10, and 14 days, respectively. Global surface CO
9 distribution are shown for 13, 7, 10, and 14 days prior to the arrival time, respectively. The deeper the color, the
10 higher the CO concentration.
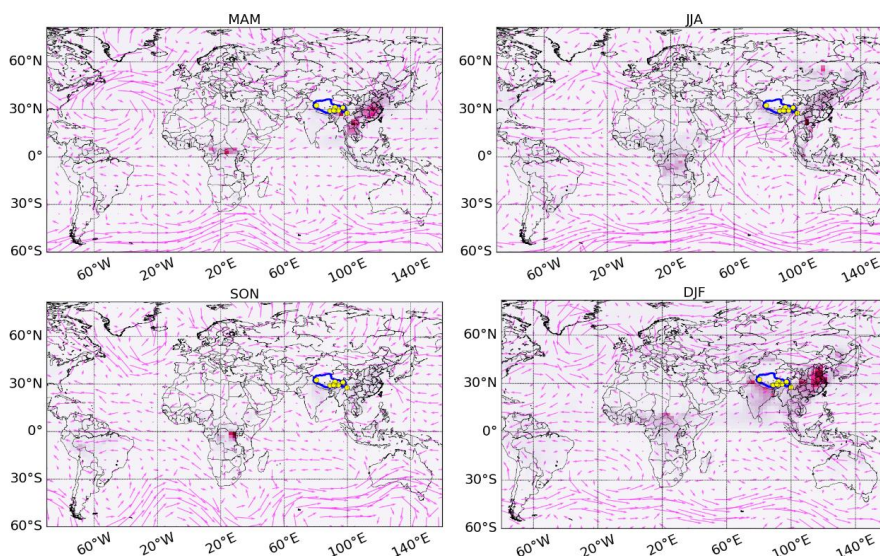
Fig. 12. Spatial distribution of CO VMR in the GEOS-Chem tagged CO simulations in different seasons, and the arrows represent the mean horizontal wind vectors at 500 hPa. The HTP and the studied regions are marked with a blue outline and yellow dots, respectively. Meteorological fields are from the GDAS-1 data.
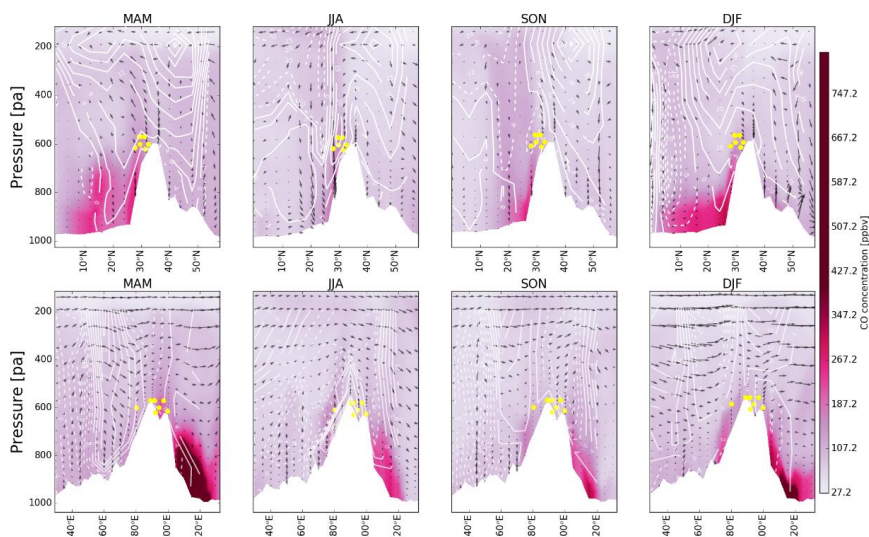
Fig. 13. The first row shows the latitude–height distributions of CO VMR averaged over 80–100° E in the tagged CO simulations in different seasons (corresponding to different columns). The white contours at intervals of 6 m s⁻¹ represent the westerly (solid) and easterly (dashed) mean meridional winds; the white area represents topography and the arrows represent the wind vectors (vertical velocity in units of 10^{-4} hPa s⁻¹ and zonal wind in m s⁻¹); the studied regions are marked with yellow dots. The second row is similar to the first row except that the quantities are on the longitude–height perspective averaged over 28–33° N. Here the white contours represent the southerly (solid) and northerly (dashed) mean zonal winds, and the horizontal component of the wind vectors is meridional wind (m s⁻¹). Meteorological fields are from the GDAS-1 data.

1 Tables

Table 1. Geolocations of measurement sites in eight cities over the HTP region. All sites are organised as a function of increasing longitude. Population statistics are prescribed from the 2018 demographic data provided by National Bureau of Statistics of China

Name	Longitude mean	Latitude mean	Altitude mean (km)	Population	Number of sites	Time period
Ngari	80.1°E	32.5°N	4.5	110,000	2	Jan. 2015 - present
Shigatse	88.9°E	29.3°N	4.0	770,000	3	Jan. 2015 - present
Lhasa	91.1°E	29.7°N	3.65	690,000	6	Jan. 2015 - present
Shannan	91.8°E	29.2°N	3.7	370,000	2	Jan. 2015 - present
Naqu	92.1°E	31.5°N	4.45	500,000	3	Jan. 2015 - present
Nyingchi	94.4°E	29.6°N	3.1	230,000	2	Jan. 2015 - present
Qamdo	97.2°E	31.1°N	3.26	700,000	3	Jan. 2015 - present
Diqing	99.7°E	27.8°N	3.38	410,000	2	Jan. 2015 - present

Table 2. Descriptions of all tracers implemented in the standard GEOS-Chem tagged CO simulation and the geographical definitions of all source regions

Type	Tracer	Description	Region	Location
Anthropogenic	anthNA	Fossil fuel + Biofuel CO emitted over the North America	172.5°W - 50.0°W; 24.0°N - 88.0°N	NA
	anthEUBA	Fossil fuel + Biofuel CO emitted over Europe and Boreal Asia	17.5°W - 72.5°E; 36.0°N - 45.0°N and 17.5°W - 172.5°E; 45.0°N - 88.0°N	EUBA
	anthSEAS	Fossil fuel + Biofuel CO emitted over Eastern Asia and Southern Asia	70.0°E - 152.0°E; 8.0°N - 45.0°N	SEAS
	anthROW	Fossil fuel + Biofuel CO emitted South America, Africa and Oceania	112.5°W - 32.5°W; 56°S - 24°N and 17.5°W -70.0°E; 48.0°S - 36.0°N and 70.0°E - 170.0°E; 90.0°S - 8.0°N	SA+AF+OCE
Biomass burning	bbSA	Biomass burning CO emitted over South America	112.5°W - 32.5°W; 56°S - 24°N	SA
	bbAF	Biomass burning CO emitted over Africa	17.5°W -70.0°E; 48.0°S - 36.0°N	AF
	bbSEAS	Biomass burning CO emitted over South Asia and East Asia	70.0°E - 152.5°E; 8.0°N - 45.0°N	SEAS
	bbOC	Biomass burning CO emitted over Indonesia and Oceania	70.0°E - 170.0°E; 90.0°S - 8.0°N	OC
	bbEUBA	Biomass burning CO emitted over Europe and Boreal Asia	17.5°W - 72.5°E; 36.0°N - 45.0°N and 17.5°W - 172.5°E; 45.0°N - 88.0°N	EUBA
	bbNA	Biomass burning CO emitted over North America	173°W - 50°W; 24.0°N - 88.0°N	NA
Oxidation	oxCH	CO chemically produced from CH_4 oxidation	global	global
	oxNMVOC	CO chemically produced from NMVOCs oxidation	global	global

1 Table 3. Statistical summary of surface CO VMR in eight cities over the HTP region. All cities are organised as a
2 function of increasing longitude.

Name	Diurnal cycle		Seasonal cycle		Interannual variability	
	Hourly min. (ppbv)	Hourly max. (ppbv)	Monthly min. (ppbv)	Monthly max. (ppbv)	Annual mean (ppbv)	Trend (% per yr)
Ngari	319.2 ± 150.6 (16:00)	556.1 ± 311.0 (11:00)	206.8 ± 93.5 (Aug.)	632.0 ± 268.2 (Jan.)	395.9 ± 138.0	-6.1 ± 1.39
Shigatse	256.4 ± 177.1 (18:00)	464.9 ± 253.1 (10:00)	274.4 ± 98.2 (Sep.)	496.8 ± 365.3 (Jan.)	408.4 ± 165.8	11.9 ± 1.38
Lhasa	334.5 ± 101.0 (17:00)	650.0 ± 430.7 (22:00)	375.8 ± 128.6 (Jul.)	759.4 ± 473.8 (Dec.)	446.1 ± 138.5	-1.49 ± 1.32
Shannan	393.1 ± 230.3 (17:00)	572.6± 265.6 (10:00)	310.5 ± 120.5 (Oct.)	665.8± 280.2 Feb.	409.8± 147.0	-3.68± 1.42
Naqu	757.3 ±411.6 (17:00)	1485.1 ± 1104.7 (23:00)	607.1 ±284.3 (Jul.)	1539.4 ± 1075.8 (Nov.)	901.6 ± 472.2	-21.6 ± 4.5
Nyingchi	286.5 ± 106.6 (6:00)	404.5 ±142.4 (10:00)	257.8 ± 123.0 (Jul.)	428.2 ±169.5 (Nov.)	318.3± 71.6	2.47 ± 0.7
Qamdo	738.4 ± 517.7 (5:00)	1326.5 ± 1048.8 (21:00)	469.3 ± 217.7 (Jul.)	1887.1 ± 1132.0 (Dec.)	766.1 ± 413.1	-17.0 ± 4.37
Diqing	455.8 ± 257.8 (5:00)	798.7 ± 427.1 (10:00)	419.0 ± 221.2 (Jul.)	793.2 ± 666.8 (May)	531.4 ± 156.8	-5.09 ± 2.19

4 *Appendix.*
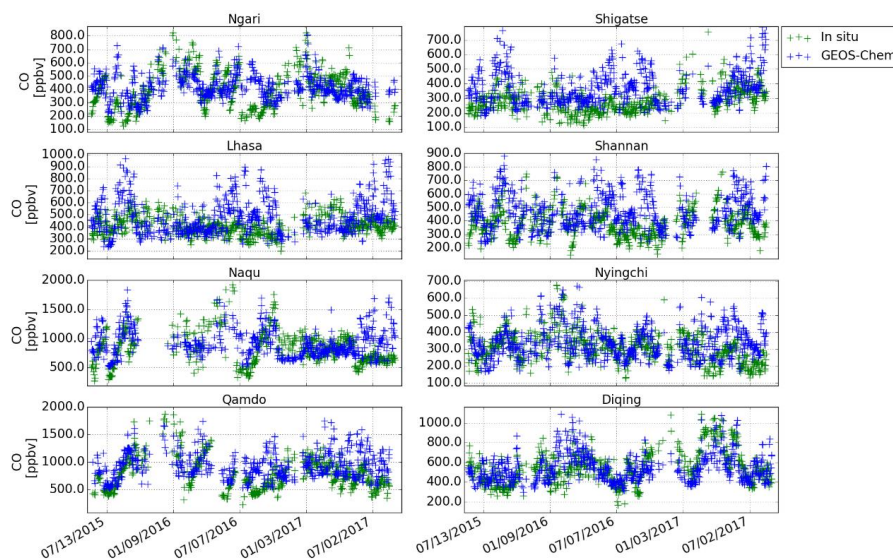
6 Fig. A1. Daily mean time series of surface CO VMR for in situ measurement and the sclaled GEOS-Chem
7 simulation over the Himalayas and Tibetan Plateau (HTP).
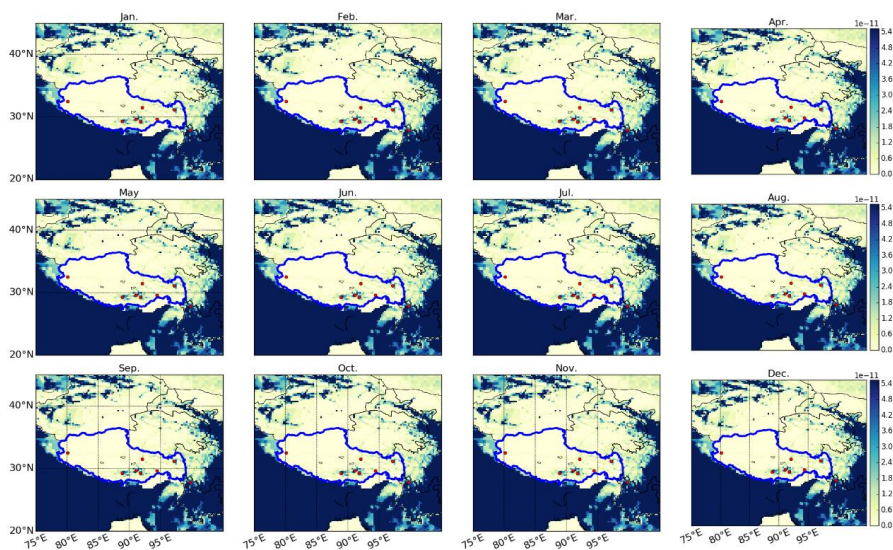
Fig. A2. Total CO emission distribution in 2017 (0.25°×0.25°) from the Multi-resolution Emission Inventory for China (MEIC) over the Himalayas and Tibetan Plateau (HTP) region and suroundings. Units are in kg/m^2/s. The HTP and the studied regions are marked with a blue outline and red dots, respectively.
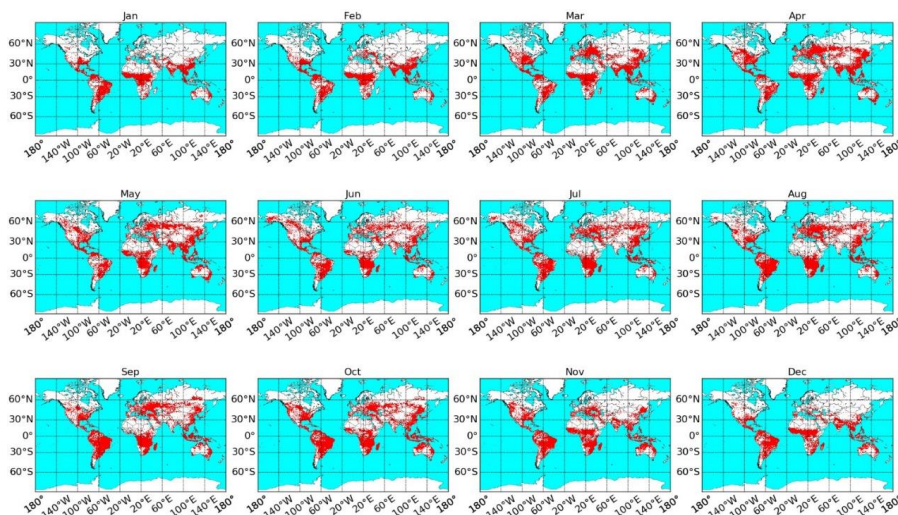
Fig. A3. Global fire distribution in January – December 2015 avaiable from the FIRMS fire atlas (https://firms.modaps.eosdis.nasa.gov/download/; Sun et al., 2020a).